Resurgent Na^+ Current Offers Noise Modulation in Bursting Neurons

[1]Sharmila Venugopal, [1]Soju Seki, [5]David H Terman, [3]Antonios Pantazis, [3]Riccardo Olcese, [4]Martina Wiedau-Pazos, [1,2]Scott H Chandler*

[1]Department of Integrative Biology and Physiology
[2]The Brain Research Institute
[3]Departments of Anesthesiology & Perioperative Medicine and [4]Neurology
David Geffen School of Medicine, University of California Los Angeles

[5]Department of Mathematics
The Ohio State University

***Editorial and manuscript correspondence to SV**
Department of Integrative Biology and Physiology
University of California Los Angeles
621, Charles E Young Drive South, LSSA 4214
Los Angeles, CA 90095
Phone: (310) 206-0332
Email: vsharmila@g.ucla.edu

pages: 31 (including online methods section)
figures: 9
words in abstract: 160
words (Introduction, Results and Discussion): 4396
references: 56

Supplementary information included as a separate file: 4 figures, 2 tables and Supplementary information including 2 pieces of model code, 1 piece of dynamic-clamp C^{++} code, and, text detailing model analysis.

Abstract

Neurons utilize bursts of action potentials as an efficient and reliable way to encode information. It is likely that the intrinsic membrane properties of neurons involved in burst generation may also participate in preserving its temporal features. Here we examined the contribution of the persistent and resurgent components of voltage-gated Na^+ currents in modulating the burst discharge in sensory neurons. Using mathematical modeling, theory and dynamic-clamp electrophysiology, we show that, distinct from the persistent Na^+ component which is important for membrane resonance and burst generation, the resurgent Na^+ can help stabilize burst timing features including the duration and intervals. Moreover, such a physiological role for the resurgent Na^+ offered noise tolerance and preserved the regularity of burst patterns. Model analysis further predicted a negative feedback loop between the persistent and resurgent gating variables which mediate such gain in burst stability. These results highlight a novel role for the voltage-gated resurgent Na^+ component in moderating the entropy of burst-encoded neural information.

Author Summary

The nervous system extracts meaningful information from natural environments to guide precise behaviors. Sensory neurons encode and relay such complex peripheral information as electrical events, known as action potentials or spikes. The timing intervals between the spikes carry stimulus-relevant information. Therefore, disruption of spike timing by random perturbations can compromise the nervous system function. In this study we investigated whether the widely-distributed voltage-gated sodium (Na^+) ion channels important for spike generation can also serve as noise modulators in sensory neurons. We developed and utilized mathematical models for the different experimentally inseparable components of a complex Na^+ channel current. This enabled phenomenological simplification and examination of the individual roles of Na^+ components in spike timing control. We further utilized real-time closed-loop experiments to validate model predictions, and theoretical analysis to explain experimental outcomes. Using such multifaceted approach, we uncovered a novel role for a resurgent Na^+ component in enhancing the reliability of spike timing and in noise modulation. Furthermore, our simplified model can be utilized in future computational and experimental studies to better understand the pathological consequences of Na^+ channelopathies.

Introduction

Real-time signal detection in uncertain settings is a fundamental problem for information and communication systems. Our nervous system performs the daunting task of extracting meaningful information from natural environments and guides precise behaviors. Sensory neurons for instance use efficient coding schemes such as bursting that aid in information processing[1]. Mathematical models of bursting have helped explain the basic structure of an underlying dynamical system as one in which a slow process dynamically modulates a faster action potential/spike-generating process, leading to stereotypical

68 alternating phases of spiking and quiescence[2, 3]. The so-called *recovery period* of the slow process governs
69 the intervals between bursts which is often susceptible to random perturbations. Uncertainty in spike/burst
70 intervals can alter the timing precision and information in a neural code[4]. Consequently, ionic mechanisms
71 that modulate the recovery of membrane potential during spike/burst intervals, can play a role in
72 maintaining the stability of these timing events and aid neural information processing. Here we examined
73 a candidate mechanism involving neuronal voltage-gated Na^+ currents for a role in the stabilization of
74 burst discharge (durations and intervals) and noise modulation.

75 Voltage-gated Na^+ currents are essential for spike generation in neurons[5]. The molecular and
76 structural diversity of Na^+ channels and the resultant functional heterogeneity and complexity, suggest
77 their role beyond mere spike generation[6]. For instance, in addition to the fast/transient Na^+ current (I_{NaT})
78 mediating action potentials, a subthreshold activated persistent Na^+ current (I_{NaP}) participates in the
79 generation of subthreshold membrane oscillations (STO) (e.g., see[7]). These oscillations can lead to
80 membrane resonance by which a neuron produces the largest response to oscillatory inputs of some
81 preferred frequency[8, 9]. Neurons utilize this mechanism to amplify *weak* synaptic inputs at resonant
82 frequencies[10]. The slow inactivation and recovery of I_{NaP} further provides for the slow process required
83 for rhythmic burst generation[11-13] and therefore can contribute to efficient information processing in
84 multiple ways. However, during ongoing activity, random membrane fluctuations can alter the precision
85 and order of burst timings which can distort/diminish the information in neural code. Here, we provide
86 evidence that a frequently observed resurgent Na^+ current (I_{NaR}), often coexistent with I_{NaP} might be a
87 mechanism by which neurons stabilize burst discharge while maintaining its order and entropy. The I_{NaR},
88 in neurons and other excitable cells is an unconventional Na^+ current which physiologically activates from
89 a *brief* membrane depolarization followed by repolarization, such as during an action potential[11, 14-17]. In
90 the well-studied neuronal Nav1.6-type Na^+ channels, such a macroscopic I_{NaR} is biophysically suggested

to occur from an open-channel block/unblock mechanism[18, 19]. Consequently, I_{NaR} is known to mediate depolarizing after-potentials and promote high-frequency spike discharge in neurons [14, 20-24]. Sodium channels containing the Nav1.6 subunits carry all three types of sodium currents and are widely distributed in the central and peripheral neurons and participate in burst generation [14, 25]. Sodium channelopathy involving alteration in I_{NaR} and I_{NaP}, and its association with irregular firing patterns and ectopic bursting in disease (e.g., [26-29]), prompted us to investigate distinct roles for these Na^+ currents in regulating bursting in sensory neurons.

Lack of suitable functional markers and experimental tools to dissociate the molecular mechanism of I_{NaR} from I_{NaP}, led us to use computational modeling and dynamic-clamp electrophysiology to examine a role for I_{NaR} in burst control; however see [19, 23, 24]. Although existing Markovian models model a single channel Nav1.6 type I_{Na} using a kinetic scheme (e.g., [30, 31]), they have limited application for studying exclusive roles of I_{NaR} and I_{NaP} in the control of neural bursting; however see[13, 23, 32, 33]. Here, we developed a novel mathematical model for I_{NaR} using the well-known Hodgkin-Huxley (HH) formalism which closely mimics the unusual voltage-dependent open-channel unblocking mechanism. We integrated the model I_{NaR} into a bursting neuron model with I_{NaP} that we previously reported to study their exclusive roles in burst control in the jaw proprioceptive sensory neurons in the brainstem Mesencephalic V (Mes V) nucleus[8]. To validate model predictions, we used *in vitro* dynamic-clamp electrophysiology, and theoretical stability analysis. Using these approaches, we identify a novel role for I_{NaR} in stabilizing burst discharge and noise modulation in these sensory neurons (see **Fig. 1** for a workflow and approaches used).

Results

We first developed a novel HH-based model for the resurgent component of a Nav1.6-type Na^+ current and combined it with our previous HH-type models for the transient and persistent Na^+ currents[8].

Although the total Na^+ current arises from a single channel[11, 30], we formulated the model I_{Na} as a sum of the three components as shown in **Fig. 2a** (also see **Methods**): the transient, I_{NaT}, the resurgent, I_{NaR}, and, the persistent, I_{NaP} current. This enabled easy manipulation of individual components to study their exclusive role in burst control. We ensured that each of these components mimic the distinct voltage-dependencies and kinetics observed during voltage-clamp recording in Mes V neurons[11, 34]. The classic I_{NaT} with fast inactivation kinetics (order of 1 ms) mediates spike generation, the persistent I_{NaP} with slow inactivation/recovery (order of 1000 ms) mediates STO and provides for the slow process responsible for rhythmic bursting in Mes V neurons[8, 35, 36], and, the resurgent I_{NaR} which mimics the phenomenology of an open channel unblock mechanism with a peak time of ~6 ms and decay kinetics on the order of 10 ms[11, 19, 30] (also see **Fig. 3**).

We compared our model I_{Na} and its components to the macroscopic I_{Na} observed in voltage-clamp recordings in Mes V neurons[11, 14] to ensure qualitative and quantitative similarities (see **Fig. 3b**). We further ensured that our I_{Na} model closely resembled the I_{Na} generated in Markovian models[30], which follow a kinetic scheme and do not formulate the three components separately (see **Supplementary Fig. 1**). Our model I_{Na} also satisfied previously described contingency of Nav1.6-type Na^+ channels carrying resurgent current: activation of I_{NaR} only up on brief depolarization followed by hyperpolarization to ~ -40 mV, and the correspondence between maximum channel availability and peak time of resurgent current[30] (see **Supplementary Fig. 2**).

We incorporated the model I_{Na} into a conductance-based single-compartment neuron model (see schematic and membrane voltage trace in black in **Fig. 2b**). Together with a minimal set of Na^+, K^+ and leak conductances, the model neuron faithfully reproduced an expected rhythmic burst discharge observed in Mes V sensory neurons; the total I_{Na} generated during action potentials is shown in expanded time in the figure (red trace). **Figure. 2c** shows the dynamic-clamp experiment in an intrinsically bursting Mes V

137 neuron. The control burst was generated by simply driving the neuron with a step depolarization, following
138 which we blocked action potential generation by bath application of tetrodotoxin (1 μM TTX) (see black
139 horizontal bar in **Fig. 2c**). Subsequently, we introduced the real-time model I_{Na} using dynamic-clamp
140 during TTX application and by adjusting the conductances of the three I_{Na} components suitably, we were
141 able to regenerate action potential bursts (see **Methods** on the choice of conductance values). The
142 dynamic-clamp I_{Na} generated during action potentials is shown in expanded time in the figure for
143 comparison with the model simulation in **Fig. 2b** (red trace).

144 **A novel HH-based mathematical model for resurgent Na^+ current**

145 As noted earlier, the total I_{Na} in our model has the novel resurgent component, I_{NaR}; the transient
146 and persistent components are similar to our previous report[8]. **Figure 3a (left panel)** illustrates a well-
147 accepted mechanism of Na^+ resurgence[30], wherein a putative blocking particle occludes an open channel
148 following brief depolarization such as during an action potential; subsequently upon repolarization, a
149 voltage dependent unblock results in a resurgent Na^+ current. Our I_{NaR} formulation recapitulates this
150 unusual behavior of Na^+ channels using nonlinear ordinary differential equations for a blocking variable
151 (b_r) and a competing inactivation (h_r) (see **Methods**). Different from a traditional activation variable of
152 an ionic current in HH models, we formulated the I_{NaR} gating using a term $(1 - b_r)$ to enable an
153 unblocking process (see I_{NaR} equation in **Methods** and in **Fig. 3a**). Here, the model variable b_r reflects
154 the fraction of channels in the blocked state at any instant, and '1' denotes the maximum proportion of
155 open channels, such that $(1 - b_r)$ represented the fraction of unblocking channels. Such a formulation
156 enabled mimicking the open-channel unblocking process as follows: Normally the b_r is maintained 'high'
157 such that $(1 - b_r)$ term is small and therefore no I_{NaR} flows, except when a spike occurs, which causes b_r
158 to decay in a voltage-dependent manner. This turns on the I_{NaR} which peaks as the membrane voltage
159 repolarizes to ~ -40 mV, following which the increasing inactivation variable h_r gradually turns off the

160 I_{NaR}. The steady-state voltage dependency of unblock, $(1 - br_{\infty}(V))$, and the competing inactivation
161 ($hr_{\infty}(V)$) in the model are shown in **Fig. 3a (middle panel)**, along with the equation for I_{NaR}; the magenta
162 shaded region highlights the voltage-dependency of I_{NaR} activation as posited to occur during open-
163 channel unblocking. In **Fig. 3a (right panel)**, we show simulated I_{NaR} (in magenta), peaking during the
164 recovery phase of spikes (in black). In **Fig. 3b (I.)**, we reproduced experimentally observed I_{Na} during
165 voltage-clamp recording and highlight the resurgent component in both model (*left*) and experiment
166 (*right*), (inset shows experimental protocol; also see legend and **Methods**). A comparative current-voltage
167 relationship for the model and experiments is shown in **Fig. 3b (II.)**; also see **Supplementary Fig. 3** for
168 detailed kinetics of model I_{NaR}. Taken together, the above tests and comparisons ensured the suitability
169 of our model for further investigation of I_{NaR} mediated burst control.

170 **Resurgent and persistent Na^+ currents offer *push-pull* modulation of spike/burst intervals**

171 Given that I_{NaR} is activated during the recovery phase of an action potential, physiologically, any
172 resulting rebound depolarization may control the spike refractory period, and increase spike frequency
173 and burst duration[22, 37]. We tested this by selectively increasing the maximal resurgent conductance g_{NaR}
174 in our model neuron simulation and validated the predictions using dynamic-clamp experiments as shown
175 in **Figs. 4a, b**. In parallel, we also exclusively modified the maximal persistent conductance g_{NaP} using
176 model simulations and verified the effects using dynamic-clamp experiments as shown in **Figs. 4c, d**. We
177 only focused on rhythmically bursting Mes V neurons and quantified the burst timing features including
178 the inter-burst intervals (IBIs), burst duration (BD) and inter-spike intervals (ISIs) as illustrated in the
179 boxed inset in **Fig. 4**. **Figure panels 4e – j** show a comparison of the exclusive effects of g_{NaR} versus
180 g_{NaP} on each of these burst features. These experimental manipulations using model currents and
181 quantification of resulting burst features revealed significant differences and some similarity between the
182 action of g_{NaR} and g_{NaP} in burst control. First, increases in g_{NaR} resulted in *longer* IBIs, which was in

183 contrast with the effects of the persistent Na^+ conductance, g_{NaP}, which *decreased* IBIs (effect highlighted
184 with red double arrows in **Figs. 4a – d** and quantified using box plots in **Figs. 4e and h**). Alternatively,
185 increasing g_{NaR} *reduced* ISIs, while g_{NaP} had the opposite effect on these events, resulting in an overall
186 *increase* in ISIs with g_{NaP} increases (see **Figs. 4f and i**); whereas g_{NaR} and g_{NaP} had similar effect in
187 increasing BDs (see **Figs. 4g and j**). Box plots in **Figs. 4e – j** show 1st, 2nd (median) and 3rd quartiles; error
188 bars show 1.5x deviations from the inter-quartile intervals. For each case (or cell), n values represented
189 events (ISI, IBI and BD) and reported here are within-cell effects for different g_{NaR} and g_{NaP} applications
190 during 20 sec step-current stimulation. For the g_{NaR} applications (or series), IBI mean ± std were 210.49
191 ± 69.33 (control, $n = 7$), 450.29 ± 116.56 (1x, $n = 26$) and 1074.06 ± 199.17 (2x, $n = 11$), and for g_{NaP}
192 applications, these values were 1448.71 ± 450.92 (control, $n = 4$), 910.10 ± 527.27 (1x, $n = 8$) and
193 644.35 ± 234.19 (1.5x, $n = 6$). For g_{NaR} series, ISI mean ± std were 20.26 ± 1.65 (control, $n = 59$), 12.56
194 ± 2.25 (1x, $n = 646$) and 10.56 ± 1.81 (2x, $n = 783$), and for g_{NaP} series these values were 12.76 ± 1.13
195 (control, $n = 159$), 12.57 ± 1.05 (1x, $n = 611$) and 13.56 ± 1.42 (1.5x, $n = 503$). For g_{NaR} series, BD
196 mean ± std were 176.36 ± 69.57 (control, $n = 8$), 300.56 ± 77.90 (1x, $n = 27$) and 671.16 ± 285.96 (2x,
197 $n = 12$), and for g_{NaP} series these values were 346.59 ± 88.39 (control, $n = 4$), 571.30 ± 197.56 (1x, $n =$
198 8) and 1334.20 ± 592.59 (1.5x, $n = 7$). Treatment effects and group statistics for all the replicates showing
199 the above effects across six Mes V bursting neurons, each from a different animal are summarized in
200 **Supplementary Table 2**. A one-way ANOVA was used to test the treatment effects of g_{NaR} and g_{NaP}
201 applications, and when significant, a *post hoc* two-sample Student t-test was used for group comparisons
202 between control and 1x, 1x and 2x, and control and 2x for g_{NaR} cases, and between control and 1x, 1x
203 and 1.5x, and control and 1.5x for g_{NaP} cases. Asterisks above box plots between groups in **Figs. 4e – j**
204 indicate $p < 0.05$ using two-sample Student t-tests for *post-hoc* comparisons. Furthermore, as shown in
205 **Fig. 4**, the model simulations predicted consistent effects (note white circles denote predicted values in

206 panels **e - j**) with dynamic-clamp experiments, making the model suitable for further analysis of I_{NaR}/I_{NaP}
207 mediated mechanism of burst control (see *white circles* in panels **4e - j**). In two additional bursting
208 neurons, we also conducted g_{NaR} and g_{NaP} subtraction experiments which showed consistent reverse
209 effects of additions (see **Supplementary Fig. 4 and legend**). In the g_{NaP} subtraction experiment, note
210 that a -2x g_{NaP} resulted in the abolition of bursting and sub-threshold oscillations as shown in the figure.
211 Such an effect was reproduced in the neuron model by setting g_{NaP} = 0, as shown in **Suppl. Fig. 4c**.

212 To test whether I_{NaR} and I_{NaP} differentially modulate the regularity and precision of spike timing
213 we observed the inter-event intervals (or IEIs) during real-time addition of g_{NaR} and g_{NaP}. As shown in
214 **Fig. 5a, b** addition of g_{NaR} improved the regularity of the two types of events: the longer IBIs and the
215 shorter ISIs, whereas, addition of g_{NaP} did not show such an effect. Note that application of real-time
216 g_{NaR} improved both the timing precision and regularity of IBIs (compare *left* and *right* panels of **Fig. 5a**),
217 while application of dynamic-clamp g_{NaP} did not seem to either of these features (compare *left* and *right*
218 panels of **Fig. 5b**). Furthermore, in **Fig. 5c** we highlight that g_{NaR} application also improved spike-to-
219 spike regularity of ISIs within bursts (shown are two representative bursts for g_{NaR} (**Fig. 5c**, *left* panel)
220 versus g_{NaP} (**Fig. 5c**, *right* panel) application from **Fig. 5a, b** (see figure legend). Taken together, these
221 opposite effects of persistent and resurgent Na^+ currents arising from a single Na^+ channel may act in
222 concert to offer a *push-pull* modulation of burst timing regulation.

223 **Resurgent Na^+ aids stabilization of burst discharge**

224 The effect of persistent g_{NaP} in reducing IBIs can be explained by its sub-threshold activation[11],
225 wherein increases in g_{NaP} *promotes* STO and burst initiation which in turn increases burst frequency and
226 reduces IBIs. Additionally, a high g_{NaP} together with its slow inactivation helps maintain depolarization
227 which can increase BDs. During spiking, I_{NaP} inactivation slowly accumulates and can contribute to any
228 spike frequency adaptation as a burst terminate. Further increases in g_{NaP} can accentuate such an effect

229 and lead to increases in spike intervals within a burst. In contrast, the rebound depolarization produced
230 due to I_{NaR} can decrease ISIs and promote spiking which prolongs the BDs. An effect which is not
231 immediately obvious is an increase in IBI due to increases in g_{NaR} since IBIs are order of magnitude
232 slower events than rise/decay kinetics of I_{NaR}. Moreover, this current is not active during IBIs. It is likely
233 that I_{NaR} which promotes spike generation produces its effect on lengthening the IBIs by further
234 accumulation of I_{NaP} inactivation during spiking and in turn reducing channel availability immediately
235 following a burst. We examined this possibility using model analysis of I_{NaR}'s effect on modulating the
236 slow I_{NaP} inactivation/recovery variable, h_p.

237 The simulated membrane potential (grey traces) and the slow I_{NaP} inactivation/recovery variable,
238 h_p (overlaid magenta traces) of the model neuron under three conditions shown in **Figs. 6a-c**: 1) with
239 default values of g_{NaR} and g_{NaP} (**Fig. 6a**), 2) an 1.5x increase in g_{NaP} (**Fig. 6b**), and, 3) a 2x increase in
240 g_{NaR} (**Fig. 6c**). The peak and trough of the slow inactivation/recovery variable, h_p correspond to burst
241 *onset* and *offset* respectively. Comparing these traces in the three panels, we note that an increase in g_{NaR}
242 effectively lowers the h_p value at which burst terminates (see curvy arrow in **Fig. 6c** and legend). This
243 observation was further supported by estimations of theoretical thresholds for *burst onset* and *offset* for
244 increasing values of g_{NaR} (**Fig. 6d**) and, similar thresholds for increasing values of g_{NaP} are provided for
245 comparison in **Fig. 6e** (see legend and **Supplementary Information** for details). Note that changes in
246 g_{NaR} did not alter the burst onset thresholds, consistent with a lack of resurgent current before spike onset
247 (see brown arrow indicating burst onset threshold in **Fig. 6d**). In contrast, increasing g_{NaR}, consistently
248 *lowered* the threshold values of slow inactivation/recovery for burst offset (see highlighted dashed box
249 with arrows pointing to the burst offset thresholds decreasing with increasing g_{NaR} values in **Fig.6d**). The
250 net effect is longer recovery time between bursts and therefore prolonged IBIs. Additionally, in **Fig. 6d**,
251 an increase in g_{NaR} extended the range of slow inactivation/recovery for which stable spiking regime

exists (marked by the green circles). This *gain in stability* is indicative of a *negative feedback loop* in the Na^+ current gating variables which model the slow inactivation and the open-channel unblock process. As shown in **Fig. 6f** (see boxed inset), during a burst, presence of a channel unblocking process and the resulting resurgent Na^+ can lead to further accumulation of slow inactivation (a positive effect) which eventually shuts off the unblocking events with further inactivation (negative feedback), which terminates a burst. The schematic on the left in **Fig. 6f** summarizes a negative feedback loop between the unblocking and slow inactivation processes of Na^+ currents which could mediate the stabilization of burst discharge as described above.

Resurgent Na^+ current offers noise tolerance

Next, we examined whether the stability of burst discharge offered by the presence of I_{NaR} can also contribute to noise tolerance. During quiescence/recovery periods between bursts, the membrane voltage is vulnerable to perturbations by stochastic influences, which can induce abrupt spikes and therefore disrupt the burst timing precision. We introduced a Gaussian noise to disrupt the rhythmic burst discharge in the model neuron when no g_{NaR} was present as shown in **Figs. 7a, b**. Subsequent addition of g_{NaR} restored burst regularity (**Fig. 7c**). Model analyses in the (h_p, V) plane provides insight into the mechanism of I_{NaR} mediated noise tolerance. Briefly, we project a portion of a (h_p, V) trajectory corresponding to the termination of one burst until the beginning of the next (see expanded insets in **Figs. 7a, b, c**) to the (h_p, V) diagrams shown in **Figs 7d, e, f** respectively (see **Supplementary Information** for details). In **Fig. 7d**, beginning at the magenta circle, the (h_p, V) trajectory (magenta trace) moves to the right as h_p recovers during an IBI, until a burst onset threshold is crossed; point where the blue circles meet the red and black curves (see **Supplementary Information** for details), and eventually bursting

begins; see upward arrow marking a jump-up in V at the onset of burst. During a burst, while V jumps up and-down during spikes, h_p moves to the left as slow inactivation accumulates during bursting (left arrow). Finally, when h_p reduces sufficiently, (h_p, V) gets closer to the burst offset threshold (points at which the green and blue circles meet), and the burst terminates (down arrow). *What is key in this figure* is that the IBI is well-defined as the time period in which the (h_p, V) trajectory moves along the red curve of steady states during the recovery process and moves past the burst onset threshold until a burst begins. However, when stochastic influences are present, the recovery period near-threshold is subject to random perturbations in V and can cause abrupt jump-up/spikes during the recovery period (see expanded inset in **Fig. 7b**). Projecting (h_p, V) during this period on to **Fig 7e**, we note that the near-threshold noise amplitudes can occasionally push the (h_p, V) trajectory (magenta) above a green region of attraction and this results in such abrupt spikes. Now, when g_{NaR} is added, the apparent restoration of burst regularity (see **Fig. 7c**) can be attributed to an expansion in this green shaded region as shown in **Fig. 7f** (see arrow pointing to a noise-tolerant region). In this situation, near-threshold random perturbations have less of an effect during the recovery process to induce abrupt spikes. *This way, the net effect of I_{NaR} on slow Na^+ inactivation prevents abrupt transitions into spiking regime following burst offset and in turn contributes to burst refractoriness and noise tolerance.* We suggest that such a mechanism can make random fluctuations in membrane potential less effective in altering the precision of bursts and therefore aid information processing.

Resurgent Na^+ moderates burst entropy

The spike/burst intervals, their timing precision and order are important for information coding[38-42]. Given our prediction that I_{NaR} can offer noise tolerance and stabilize burst discharge, we examined whether it can reduce uncertainty in spike/burst intervals and restore order in burst discharge. We tested this using model simulations and dynamic-clamp experiments as shown in **Fig. 8a - d**. In both cases, as

shown by spike raster plots in **Figs. 8e** and **f**, we disrupted the inter-event intervals (IEIs) by additive White/Weiner noise input while driving rhythmic burst discharge using step depolarization (also see **Methods**). Subsequent addition of g_{NaR} conductance restored the regularity of rhythmic bursting. We used Shannon's entropy as a measure of uncertainty in IEIs and show that increases in entropy due to noise addition was reduced to control levels by subsequent increases in g_{NaR} as shown in **Fig. 8g** (see **Methods**). We also quantified the Coefficient of Variation (CV) and noted that adding noise which shortened IBIs, indeed decreased the CV, due to a reduction the standard deviation (s.d.) of the IEI distribution. Subsequent addition of I_{NaR}, which significantly lengthened the IBIs, resulted in increases in CV values due to an increase in IEI s.d. Taken together, I_{NaR} moderated burst entropy and improved the regularity of spike/burst intervals.

Discussion

Using a combination of mathematical modeling and simulations, theory and dynamic-clamp electrophysiology, we demonstrate a novel role for voltage-gated Na^+ currents in burst control, noise modulation and information processing in sensory neurons. While the subclasses of Na^+ currents presented here are experimentally inseparable, our phenomenological simplification using the HH-formalism with *in silico knock-in* of each Na^+ current component using dynamic-clamp experiments, allowed examination of their individual contributions to burst control. Additionally, theoretical analysis suggested a putative negative feedback loop between the persistent inactivation and resurgent unblocking processes of the Nav1.6 Na^+ channels. These results portend the apparent consequences on burst control and signal processing capacity of neurons when these currents are present.

Stabilization of burst discharge by I_{NaR}

In contrast with I_{NaP}, which drives near threshold behavior and burst generation, I_{NaR} facilitated slow channel inactivation as bursts terminate (also note[11]). Increased channel inactivation due to I_{NaP} in

turn prolonged the recovery from inactivation required to initiate subsequent burst of activity. Such an interaction between open-channel unblock process underlying I_{NaR}, and, the slow inactivation underlying I_{NaP}, offer a closed-loop *push-pull* modulation of ISIs and IBIs. Specifically, presence of I_{NaR} facilitates slow Na^+ inactivation as shown by our theoretical analyses of model behavior; such enhanced slow channel inactivation can eventually shut off channel opening and unblocking. This resulted in burst stabilization. Theoretically, this represented an enlarged separatrix (or boundary) for transitioning from a sub-threshold non-spiking behavior to spiking behavior (see enlarged green shaded region in **Fig. 7f**), and the neuron becomes refractory to burst generation and hence offers noise tolerance.

Is this apparent effect of I_{NaR} physiologically plausible? Biophysical studies indicate that recovery from fast inactivation is facilitated in sodium channels that can pass resurgent current[30]; as shown here, this appears to be true for recovery from slow inactivation as well. Consistently, in the SCN8a knockout Med mouse, which lack the Nav 1.6 sodium channel subunit, recordings from mutant cells showed an absence of maintained firing during current injections, limited recovery of sodium channels from inactivation, and failure to accumulate in inactivated states. This is attributed to a significant deficit in I_{NaR} [11, 20, 37]. Furthermore, maintained or repeated depolarization can allow a fraction of sodium channels in many neurons to enter inactivation states from which recovery is much slower than for normal fast inactivation (reviewed in[43]). Here, our simulations and model analyses predict that the presence, and increase in I_{NaR} conductance, provides for a such a physiological mechanism to maintain sustained depolarization and promote fast and slow Na^+ inactivation.

Sodium currents and signal processing in neurons

Neuronal voltage-gated Na^+ currents are essential for action potential generation and propagation[5]. However, to enable fight-or-flight responses, an overt spike generation mechanism must be combined with *noise modulation* to extract behaviorally relevant inputs from an uncertain input space. Here we show

344 that, the voltage-gated Na^+ currents can serve an important role in neural signal processing (see summary
345 in **Fig. 9**). As shown in the figure, a sub-threshold activated persistent Na^+ current contributes to membrane
346 resonance, a mechanism of bandpass filtering of preferred input frequencies[9]. We call this type of input
347 gating, which is widely known to be important for brain rhythms[9, 41], a *tune-in* mechanism (see figure
348 legend). In some cases ambient noise or synaptic activity can amplify weak inputs and promote burst
349 generation[44, 45]. This way, a tune-in mechanism such as the persistent Na^+ current can contribute to weak
350 input detection and promote burst coding[46, 47]. Then again, during rhythmic bursting, presence of resurgent
351 Na^+ maintains the order and precision of the timing events of bursts while preventing abrupt transitions
352 into spiking phase due to stochastic influences as shown here. During ongoing sensory processing, such
353 burst timing regulation can provide for noise cancellation or what we call a *tune-out* mechanism, which
354 can mitigate random irregularities encoded in bursts (see **Fig. 9** and **legend**). Whether this leads to
355 improved sensory processing in the presence of natural stimuli and/or sensorimotor integration during
356 normal behaviors needs to be validated. Our biological prediction here that a sensory neuron can utilize
357 these voltage-gated Na^+ currents as a *tune-in-tune-out* mechanism to gate preferred inputs, attenuate
358 random membrane fluctuations and prevent abrupt transitions into spiking activity supports such a putative
359 role.

360 **Figures and Legends**

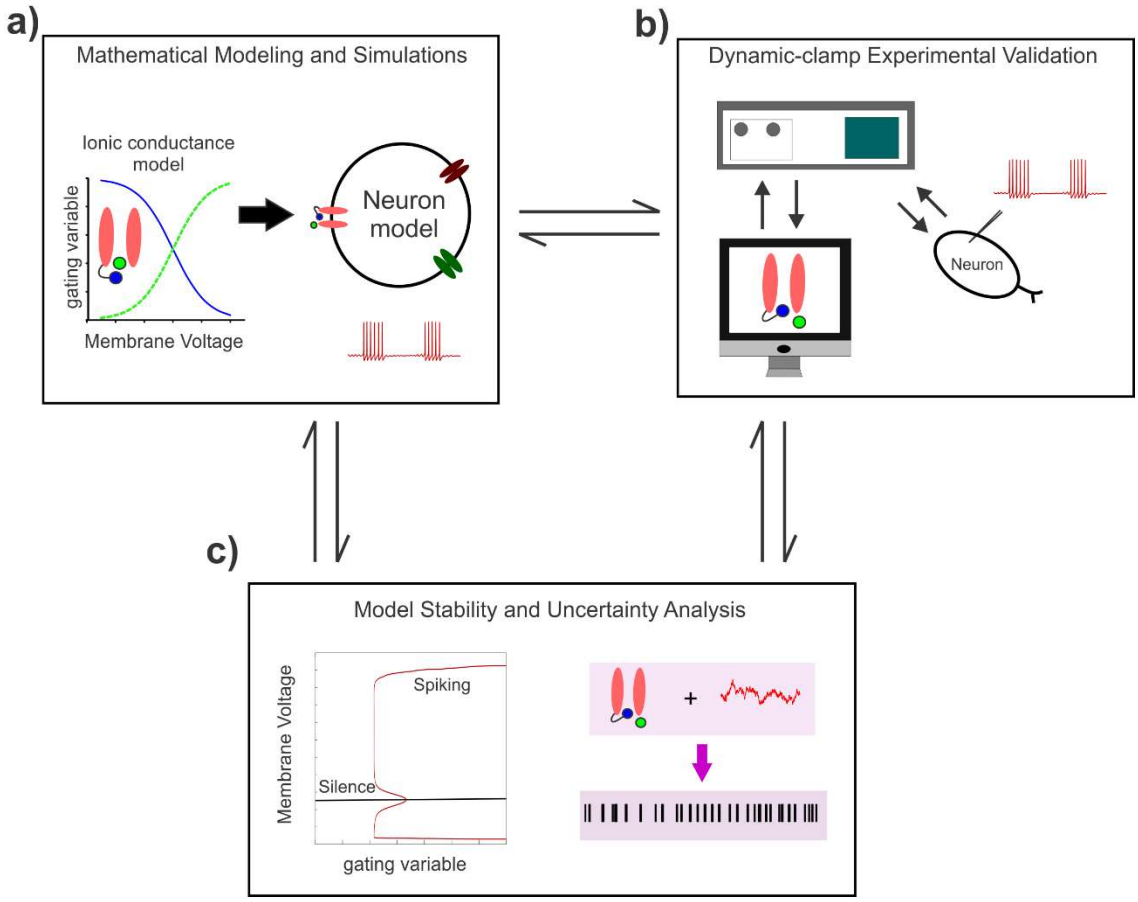

Figure 1. A workflow showing the study components and approaches. a) Development of a mathematical model for the Nav1.6-type Na^+ current components and its incorporation into a minimal conductance-based model for a bursting neuron. **b)** Dynamic-clamp validation of model predictions in the brainstem proprioceptive sensory Mes V neurons. **c)** The observed effects on neural discharge are explained using theoretical stability and uncertainty analyses.

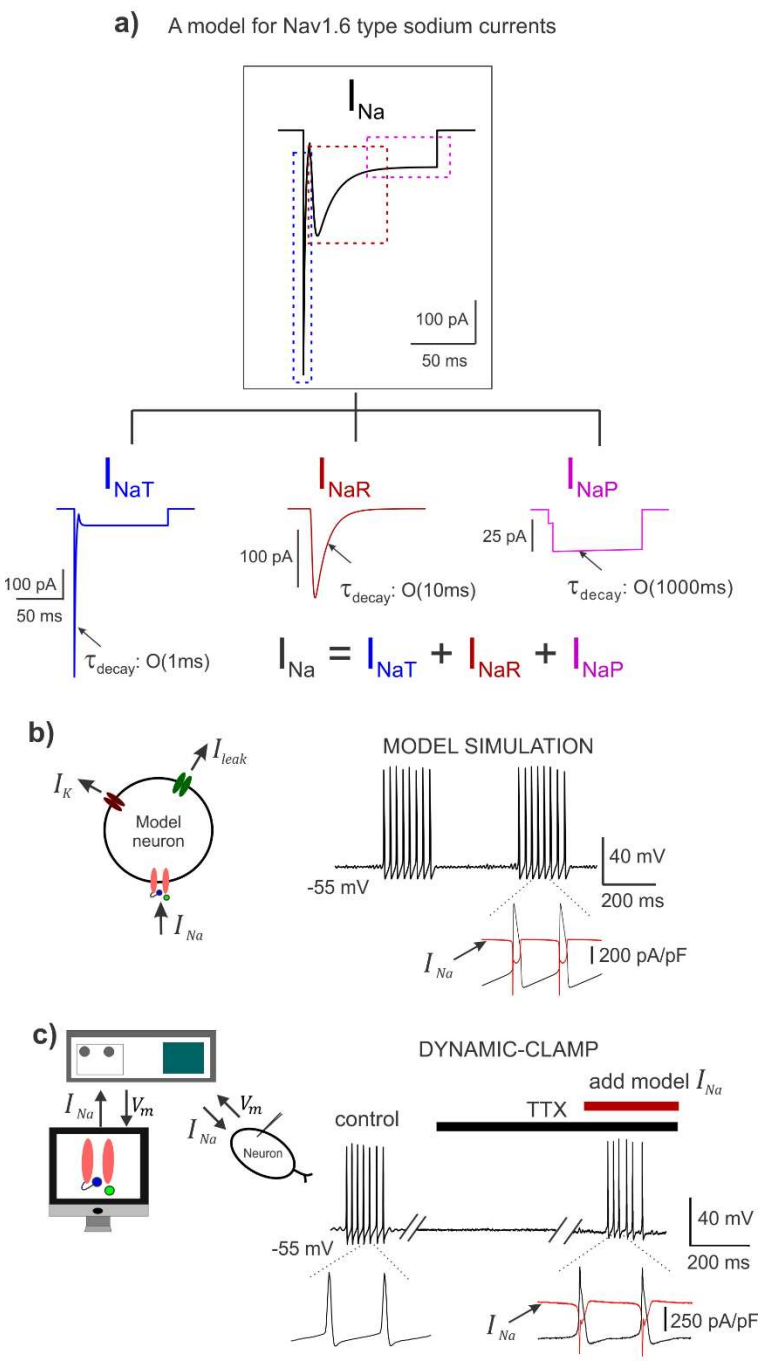

Figure 2. A Hodgkin-Huxley model for the Nav1.6 Na^+ current with the three components. a) A simulated trace showing total I_{Na}; the tree map shows each of the three components: transient I_{NaT}, resurgent I_{NaR}, and, persistent I_{NaP}; These are also highlighted by the color-matched dashed boxes in the top panel. The τ_{decay} shows the order of magnitude of the decay kinetics of the three components. **b)** *Left:* A schematic showing a conductance-based minimal model for a bursting neuron with the I_{Na} incorporated; other ionic currents in the model include a delayed-rectifier potassium (I_K) and a leak current (I_{leak}). *Right:* Model simulation demonstrates rhythmic burst discharge and inset highlights the I_{Na} current in the

model during action potentials, in red. **c)** *Left:* Schematic shows the dynamic-clamp experimental approach; V_m is the membrane potential. *Right*: Membrane potential recorded from a rhythmically bursting sensory neuron; action potentials were blocked using 1 μM TTX, and dynamic-clamp model I_{Na} was applied to regenerate spikes; double slanted lines indicate break in time; inset highlights the dynamic-clamp I_{Na} in red, during action potentials.

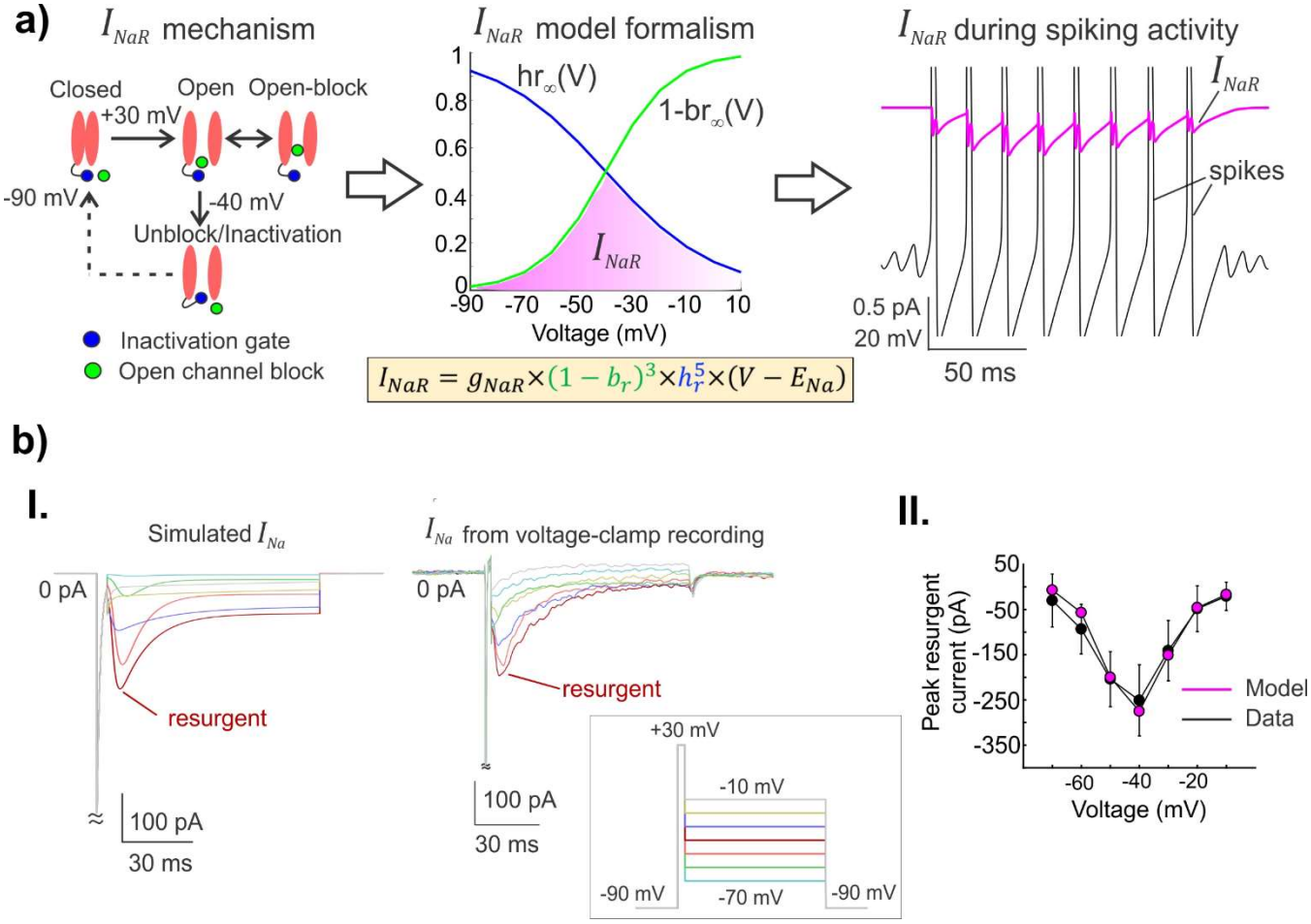

Figure 3. A novel mathematical model for the unusual resurgent component of the Nav1.6-type Na^+ current. a) *Left:* A schematic showing the voltage-dependent operation of a Na^+ channel mediating resurgent current; open-channel block/unblock (green circle); classic inactivation gate (blue ball and chain). *Middle:* The steady-state voltage-dependencies of open-channel unblocking $(1 - br_\infty(V))$ and a competing inactivation process $hr_\infty(V)$ for the novel resurgent component are shown (also see **Methods** and **Results**); the magenta shaded region highlights the voltage range over which I_{NaR} can be observed during open-channel unblocking. The equation for I_{NaR} is shown with novel blocking (b_r), and inactivation (h_r) gating variables. *Right:* The simulated I_{NaR} (in magenta) with peaks occurring during the repolarization phase of action potentials (in black) is shown. **b) I.** A comparison between simulated I_{Na} and experimentally generated I_{Na} from voltage-clamp recording is shown; boxed inset shows the experimental protocol typically used to test for voltage-dependent activation of I_{NaR}. **II.** Graphs show the

nonlinear current-voltage relationship of peak resurgent current in the model (magenta) and average peak resurgent currents measured from voltage-clamp experiments (black); error bars show standard deviation (n = 5 neurons from 5 animals).

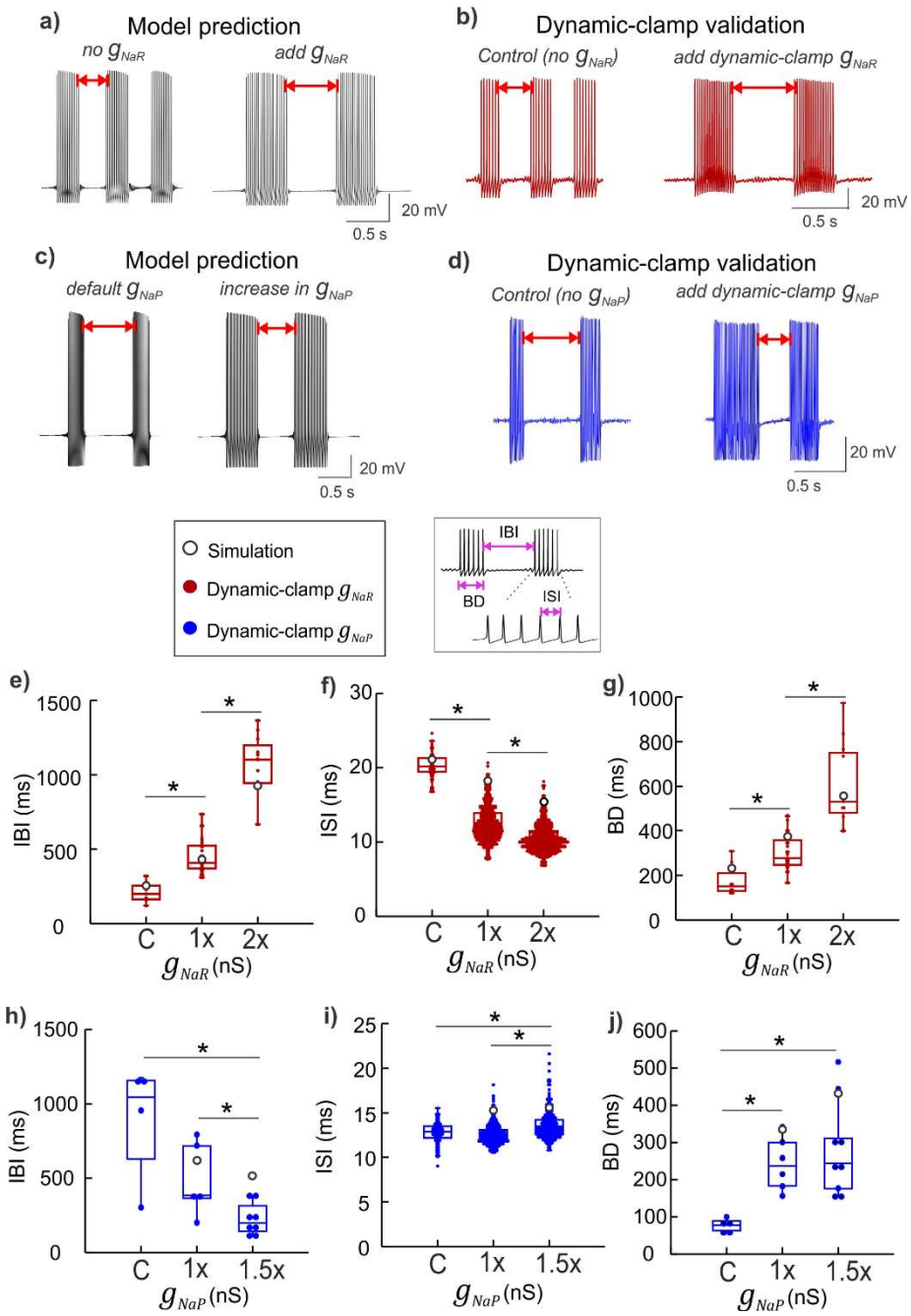

Figure 4. Physiological consequences of I_{NaR} and I_{NaP} on burst discharge. a, c) Simulated membrane voltage demonstrating the effect of g_{NaR} addition **(a)**, and g_{NaP} increase **(c)** on burst discharge. **b, d)** Dynamic-clamp experimental traces showing effects of real-time addition of g_{NaR} **(b)** and g_{NaP} **(c)** in intrinsically bursting sensory neurons; the red double arrows highlight the opposite effects of increases in

g_{NaR} and g_{NaP} on inter-burst intervals in panels **(a – d)**. The boxed inset (*left*) indicates color coding of traces for panels **e – j**. The boxed inset (*right*) highlights burst features quantified in panels **(e – j)**: inter-burst intervals (IBI), burst duration (BD), and inter-spike intervals (ISI. **e – j)** Box plots showing IBIs **(e, h)**, BDs **(f, i)**, and ISIs **(g, j)** for application of a series of g_{NaR} or g_{NaP} conductance values (see **Results** for statistics). Model values of 1x g_{NaR} and g_{NaP} are adjusted to match experimental data for 1x application of the corresponding conductance tested; C is control, values of g_{NaR} used for dynamic-clamp are 2 and 4 nS/pF for 1x and 2x respectively, and, values of g_{NaP} used are 0.25 and 0.375 nS/pF for 1x and 1.5x respectively. Asterisks indicate a $p < 0.05$ using a Student t-Test for group comparisons.

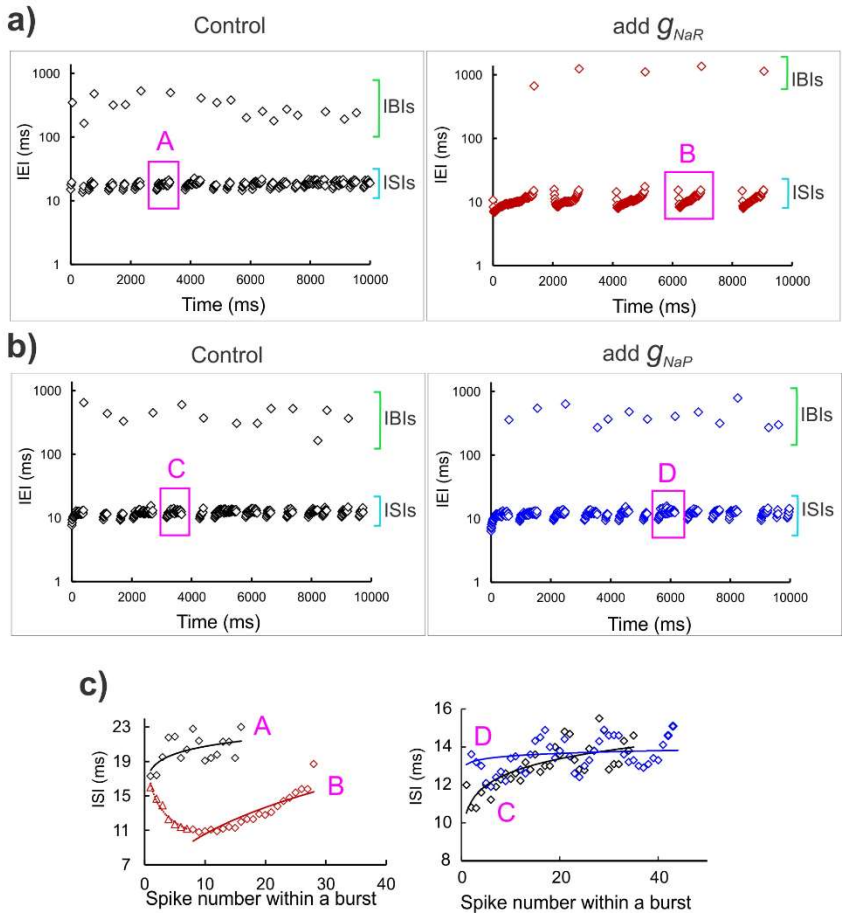

Figure 5. Spike timing regularity monitored by I_{NaR}. a, b) Time series graphs showing inter-event intervals (IEIs) under control condition (*left panels* in both **a, b**), and dynamic-clamp addition of g_{NaR} (*right panel* in **a**), and g_{NaP} (*right panel* in **b**). The green and cyan square brackets in each panel highlight the IBI and ISI range respectively. The y-axis shows IEIs on a log scale. Magenta boxes demarcate a representative burst in each case, which is expanded in the graphs in **c)**, corresponding with the bold letters, A, B, C and D. The solid lines in **(c)** are power regression fit in each case; in all the panels, black open diamonds are control, maroon open diamonds correspond with g_{NaR} application and blue open diamonds correspond with the g_{NaP} application.

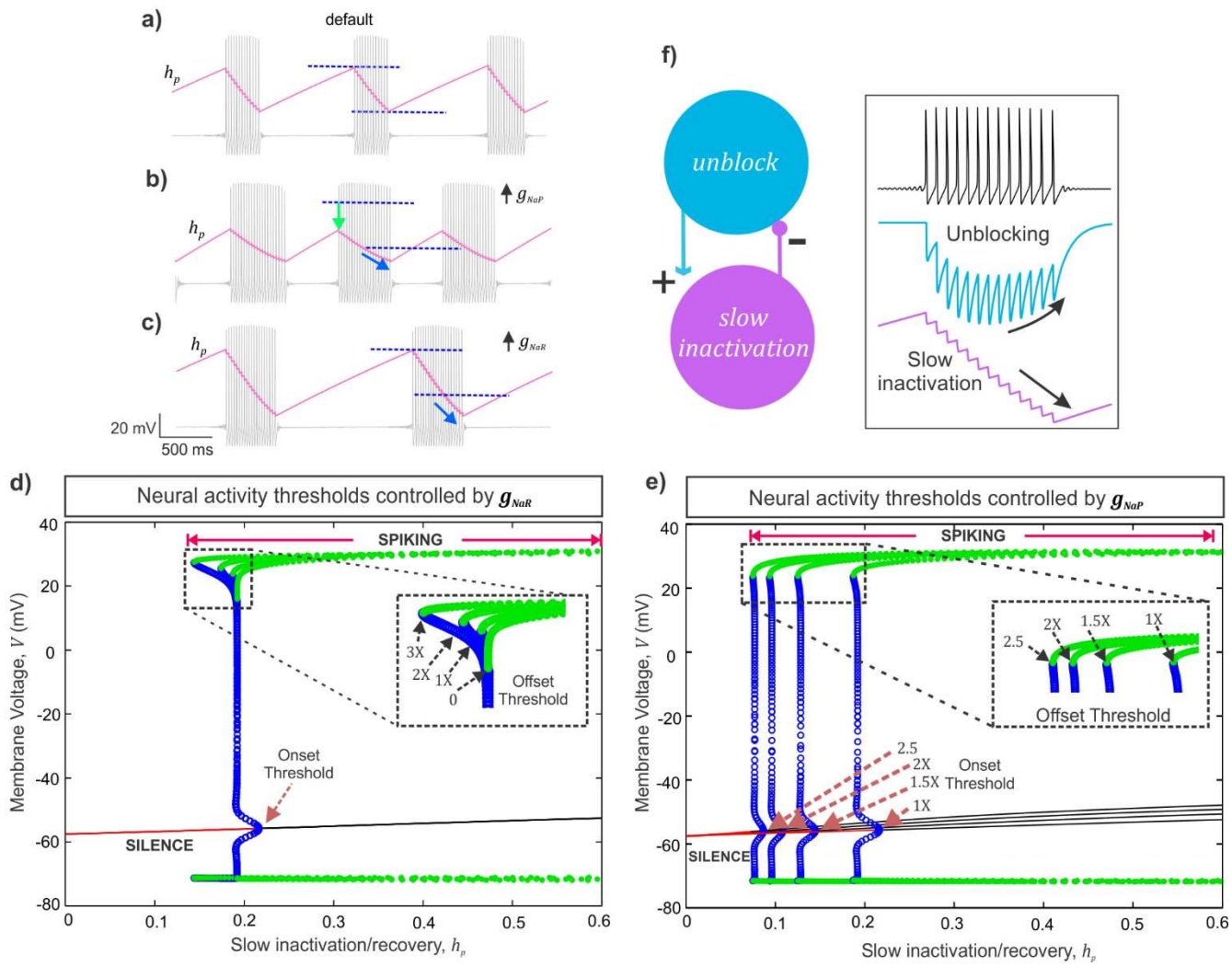

Figure 6. Analysis of a mechanism of action of I_{NaR} and I_{NaP}. a-c) The slow I_{NaP} inactivation/recovery variable, h_P is overlaid (magenta) on membrane voltage traces (grey) under default **(a)**, 1.5x g_{NaP} **(b)**, and 2x g_{NaR} **(c)** conditions; the dark blue dashed lines in **(a-c)** indicate the maximum and minimum values of the persistent inactivation variable under default condition; the light green arrow in **(b)**, highlights a reduced peak recovery required for burst onset; the light blue curvy arrows in **(b, c)** indicate further accumulation of slow inactivation before burst termination. **d, e)** Bifurcation diagrams showing the steady states and spiking regimes of the membrane voltage (V) and slow I_{NaP} inactivation/recovery (h_p). The red solid lines represent resting/quiescence states consistent with low values of h_p. The meeting points of stable equilibria (red) and unstable equilibria (black solid lines) represents the theoretical threshold for burst onset, the Hopf bifurcation point (see **Supplementary Text**). The blue open circles are the unstable periodics that form region of attraction on either side of the stable equilibria for sub-threshold membrane voltage oscillations; the meeting point of the curve of unstable periodics with the stable periodics (green filled circles) represents the theoretical threshold for burst offset/termination, saddle node of periodics (see **Supplementary Text**). The dashed boxes in **(d)** and **(e)** magnify the burst offset thresholds due to

increases in g_{NaR} **(d)** and g_{NaP} **(e)**; brown dashed arrows in **(e)** highlight shifts in burst onset thresholds due to g_{NaP} increases; 1X g_{NaR} = 3.3 nS/pF and 1X g_{NaP} = 0.5 nS/pF.

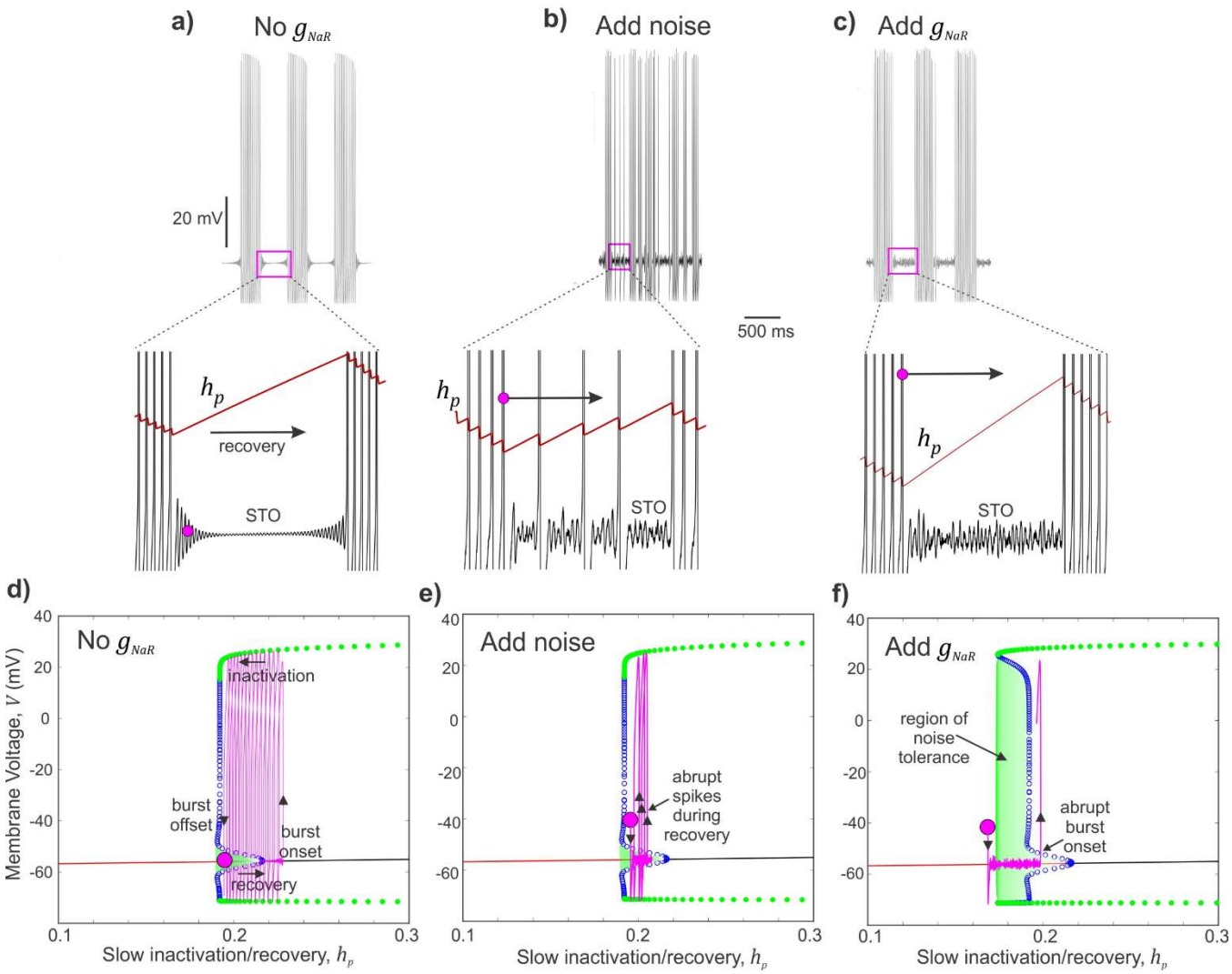

Figure 7. Resurgent Na⁺ current offers burst stability and noise modulation. a - c) Simulated membrane voltage shows neural activity patterns without any g_{NaR} **(a)**, with additive Gaussian noise input **(b)**, and with subsequent addition of g_{NaR} **(c)**. Expanded regions in **(a-c)** show membrane voltage sub-threshold oscillations (STO) during an inter-burst interval. Also overlaid is the evolution of the slow sodium inactivation/recovery variable; arrow indicates recovery during IBI, and magenta circle marks an arbitrary time point used to track these trajectories in **(d - f)**. **d - f)** Bifurcation diagrams with projected trajectories of (h_∞, V), shown in magenta to highlight the effect of addition of noise near sub-threshold voltages **(e)** and then the enlarged region of noise tolerance (highlighted green shaded region) due to addition of g_{NaR} in **(f)**. The magenta circle marks the beginning time points of each trajectory.

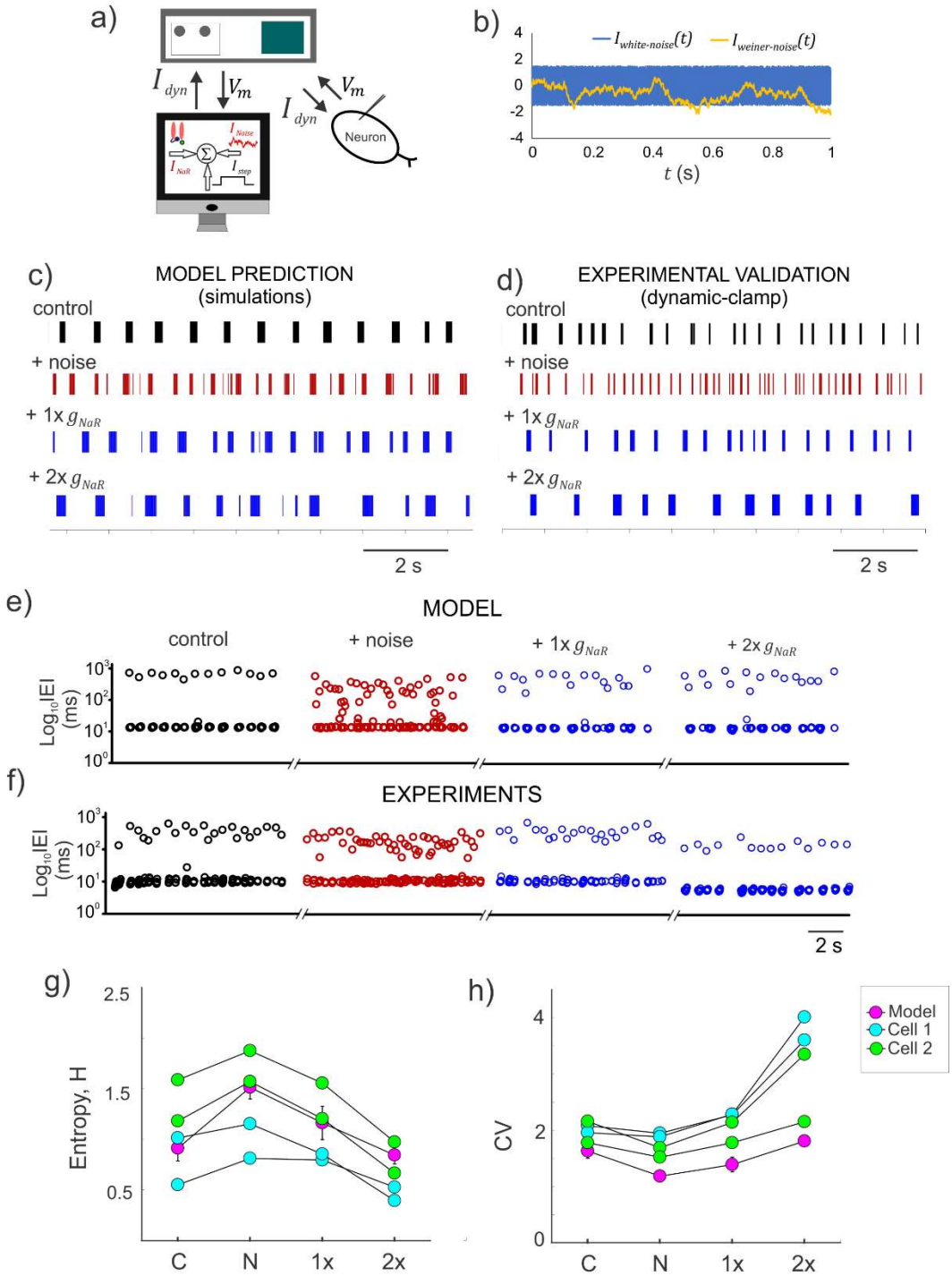

Figure 8. Resurgent Na⁺ current moderates the entropy of burst discharge. a) Schematic showing the experimental setup for real-time application of I_{NaR} and a stochastic input, I_{Noise} (see **Methods**); the dynamic-clamp current, I_{dyn} is the instantaneous sum of I_{NaR}, a step current (I_{step}) and I_{Noise}. **b)** Simulated time series of two stochastic noise profiles used to disrupt the rhythmic burst discharge in Mes V neurons; $I_{white-nois}$ was generated from a uniformly distributed random number and $I_{weiner-noise}$ was

generated from a normally distributed random number (see **Methods**). **c – d)** Raster plots showing patterns of inter-event intervals (IEIs) for the different conditions shown in the model **(e)**, and during dynamic-clamp **(f)**. **e – f)** Time series of IEI shown on a log scale for the different conditions shown in the model **(e)**, and during dynamic-clamp **(f)**. **g – h)** Shannon entropy (H) and coefficient of variability (CV) measured for IEIs under the different conditions presented in **(c)** and **(d)**. Plotted circles for the model represent an average across 10 trials, while individual trials are presented for the data points from two cells. In both **(g)** and **(h)**, C: control, N: after addition of random noise, 1x and 2x are supplements in g_{NaR} values.

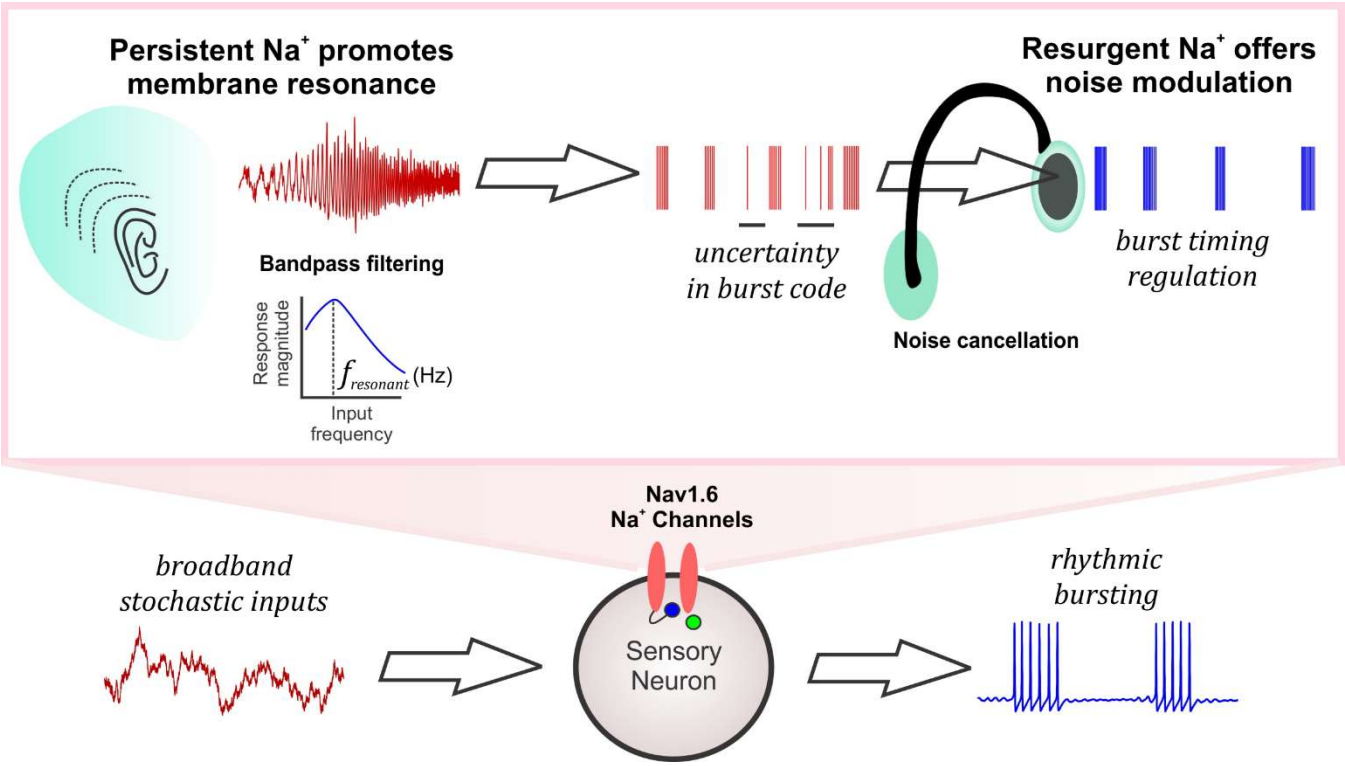

Figure 9. A consolidated role for persistent and resurgent Na^+ currents in information processing. The schematic shows the broadband input space of a sensory neuron which can produce rhythmic bursting activity. The Nav1.6-type Na^+ channels mediating the persistent Na^+ current (schematized as a listening ear) enhance neuronal resonance and tune in relevant input frequencies by bandpass filtering ($f_{resonance}$ refers to the resonant frequency of the neuron). Such selected inputs carrying behaviorally relevant stimuli are encoded as bursts but may be prone to uncertainty due to intrinsic or extrinsic stochastic influences. The resurgent Na^+ current mediated by the Nav1.6 Na^+ channels improve the regularity of spike/burst timing by mitigating the effects of noise by tuning out random spikes between bursts (schematized as a noise cancelling headphone), thus aiding in neural signal processing.

Acknowledgements

We are grateful to Dr. Bruce Bean, Dr. Christopher Del Negro and Dr. Alan Garfinkel for helpful comments on an earlier version of the manuscript.

Methods

Neuron model for bursting activity

The conductance-based Mes V neuron model that we used to investigate the physiological role for I_{NaR} and I_{NaP} components of I_{Na} in burst discharge, incorporates a minimal set of ionic conductances essential for producing rhythmic bursting and for maintaining cellular excitability in these neurons [8]. These include: 1) a potassium leak current, I_{leak}, 2) sodium current, I_{Na} as described above, and, 3) a 4-AP sensitive delayed-rectifier type potassium current (I_K) [8, 48]. The model equations follow a conductance-based Hodgkin-Huxley formalism [5] and are as follows.

$$V' = \left(-I_{Na} - I_K - I_{leak} + I_{app}\right)/C$$

$$h_t' = \frac{ht_\infty(V) - h_t}{\tau_t}$$

$$h_p' = \frac{hp_\infty(V) - h_p}{\tau_p(V)}$$

$$b_r' = \alpha_b(1 - b_r)br_\infty(V) - k_b\beta_{br}(V)b_r$$

$$h_r' = \alpha_{hr}(V)hr_\infty(V) - 0.8\beta_{hr}(V)h_r$$

$$n' = \frac{n_\infty(V) - n}{\tau_n}$$

In what follows, we provide the formulation for each of the ionic currents and describe in detail, the novel I_{NaR} model.

A. *Voltage-gated sodium currents*

In vitro action potential clamp studies in normal mouse Mes V neurons, and voltage-clamp studies in Nav1.6 subunit SCN8a knockout mice have demonstrated existence of three functional forms of the total sodium current, I_{Na}, including the transient (I_{NaT}), persistent (I_{NaP}) and resurgent (I_{NaR}) components [11, 14]. Each of these currents are critical for Mes V electrogenesis including burst discharge, however, their

exclusive role is yet unclear. Lack of suitable experimental model or manipulation to isolate each of these TTX-sensitive components, led us to pursue an alternative approach involving computational model development of the physiological I_{Na}. To further allow model-based experimental manipulation of individual components of the I_{Na}, we designed a conductance-based model as follows. Although a single Nav1.6 channel can produce all three I_{Na} components observed experimentally, we used a set of three HH-type conductances, one for each of the transient, the persistent, and the resurgent components. This allowed us to easily manipulate these components independently to test their specific role in neural burst control. The equation for the total sodium current can be written as:

$$I_{Na} = I_{NaT} + I_{NaR} + I_{NaP}$$

where,

$$I_{NaT} = \boldsymbol{g_{NaT}}(m_{t\infty}(V)h_t)(V - E_{Na})$$

$$I_{NaR} = \boldsymbol{g_{NaR}}((1 - b_r)^3 h_r^5)(V - E_{Na})$$

$$I_{NaP} = \boldsymbol{g_{NaP}}\big(m_{p\infty}(V)h_P\big)(V - E_{Na})$$

The maximal persistent conductance, g_{NaP} was set 5-10% of the transient, g_{NaT}[49] and the resurgent was set to 15-30% of g_{NaT}, based on the relative percentage of maximum I_{NaR} and I_{NaT} as revealed by voltage-clamp experiments shown in **Fig. 3**; E_{Na} is the Na^+ reversal potential.

Based on experimental data, the gating function/variable, $m_{t\infty}(V)$, and h_t, for I_{NaT}, and, $m_{p\infty}(V)$, and, h_P, for I_{NaP} are modeled as described in [8]. The rate equations for the inactivation gating variables h_t, and, h_P, model the fast and slow inactivation of the transient and persistent components respectively. The activation gates are steady-state voltage-dependent functions, consistent with fast voltage-dependent activation of I_{Na}.

Steady-state voltage-dependent activation and inactivation functions of *transient* sodium current respectively include:

$$mt_\infty(V) = \frac{1}{1+e^{\left(-(V+35)/4.3\right)}}; \qquad ht_\infty(V) = \frac{1}{1+e^{\left((V+55)/7.1\right)}}$$

Steady-state activation, inactivation and steady-state voltage-dependent time constant of inactivation for *persistent* sodium current respectively include:

$$mp_\infty(V) = \frac{1}{1+e^{\left(-(V+5\ )/6.4\right)}}; \qquad hp_\infty(V) = \frac{1}{1+e^{\left((V+52)/14\right)}}; \tau_p(V) = 100 + \frac{10000}{1+e^{\left((V+60)/10\right)}}$$

The novel I_{NaR} formulation encapsulates the block/unblock mechanism using a block/unblock variable (b_r), and, a second hypothetical variable for a competing inactivation, which we call, h_r. We call this a *hybrid* model, to highlight the fact that the model implicitly incorporates the history or state-dependent sodium resurgence, following a transient channel opening, and combines this into a traditional Hodgkin-Huxley type conductance-based formulation. In the b_r' and h_r' rate equations for b_r, and, h_r, the block/unblock variable, b_r increases or grows according to the term, $\alpha_b(1-b_r)br_\infty(V)$, and decays as per the term, $k_b\beta_{br}(V)b_r$, described as follows:

$\boldsymbol{\alpha_b(1-b_r)br_\infty(V)}$: In this growth term, we incorporate state-dependent increase in b_r, as follows; we assume that the rate of increase in b_r is proportional to the probability of channels currently being in the open state, with a rate constant, α_b which we call 'rate of unblocking'; such probability is a function of the membrane voltage given by, $br_\infty(V)$, defined as below:

$$br_\infty(V) = \frac{1}{1+e^{\left((V+40)/12\right)}}$$

The term $\left(1-br_\infty(V)\right)$, models the steady-state voltage-dependency guiding the unblocking process. The channels being in open state is represented by the term, $(1-b_r)$. Note that if $(1-b_r)$ is close to 1, this means that larger proportion of channels are in an open state, and therefore b_r grows faster, promoting blocking. We modeled $br_\infty(V)$ as a decreasing sigmoid function, such that, at negative

membrane potentials, channels have a high probability to enter future depolarized states and therefore, $(1 - b_r) \sim 0$, in turn, b_r does not grow fast.

$\boldsymbol{k_b \beta_{br}(V) b_r}$**:** In this decay term, we assume that the rate of decay of b_r, is proportional to the probability of channels being in the blocked state, with a constant of proportionality k_b, and, this probability is given by a voltage-dependent function, $\beta_{br}(V)$, defined as below:

$$\beta_{br}(V) = \frac{2}{1 + e^{\left(-(V-40)/8\right)}}$$

Note that, $\beta_{br}(V)$ gives a high probability at depolarized potentials, indicating a blocked state and enables decrease in b_r in subsequent time steps.

Taken together, b_r, represents a phenomenological implementation of a previously described block/unblock mechanism of a cytoplasmic blocking particle[19] (see schematic of channel gating in **Fig. 3a**). Additionally, a hypothetical competing inactivation variable, h_r, sculpts the voltage-dependent rise and decay times and peak amplitude of sodium resurgence at -40 mV following a brief depolarization (i.e., transient activation), as observed in voltage-clamp experiments (see **Fig. 3b**). The functions, $\alpha_{hr}(V), \beta_{hr}(V)$ and $hr_\infty(V)$ are defined as voltage-dependent rate equations that guide the voltage-dependent kinetics and activation/inactivation of the I_{NaR} component as given below.

The steady-state voltage-dependency of the competing inactivation necessary to generate a *resurgent* Na^+ current is defined as follows:

$$hr_\infty(V) = \frac{1}{1 + e^{\left((V+40)/20\right)}}$$

The voltage-dependent rate functions of such inactivation is defined by two functions as follows:

$$\alpha_{hr}(V) = \frac{1}{1+e^{\left(-(V+40)/8\right)}}; \qquad \beta_{hr}(V) = \frac{0.5}{1+e^{\left(-(V+40)/15\right)}}$$

The steepness of the voltage-dependent sigmoid functions for activation and inactivation were tuned to obtain the experimentally observed I_{NaR} activation (see **Fig. 3**; also see [11, 14, 30]). To obtain the kinetics (rise and decay times) of I_{NaR} comparable to those observed during voltage-clamp experiments (see **Supplementary Fig. 3**), the model required three units for the blocking variable $((1-b_r)^3)$ and five units for the inactivation variable (h_r^5) (see I_{NaR} equation). Together, the modeled I_{Na} reproduced the key contingencies of the Nav1.6 sodium currents (see **Supplementary Fig. 2**) [18, 30, 50].

Sensitivity analyses was conducted for the key parameters of I_{NaR} gating including α_b, and, k_b. Note that these two parameters control the rate of blocking. As expected, increasing α_b, that controls rate of increase in b_r, decreased the peak amplitude of I_{NaR}, similar to an experimental increase in block efficacy by a β-peptide (e.g., [19]). On the other hand, k_b also moderates b_r, and increasing k_b, enhances b_r decay rate, that significantly enhanced I_{NaR}, and, therefore burst duration (not shown). Large increases in k_b significantly enhanced I_{NaR} , and indeed transformed bursting to high frequency tonic spiking. However, the effects of I_{NaR} on bursting described in the results section were robust for a wide range of values of these parameters (>100% increase from default values), and, for our simulations, the range of values, $\alpha_b = 0.08\ to\ 0.1$, $k_b = 0.8\ to\ 1.2$, were used to reproduce Mes V neuron discharge properties. To reproduce experimentally observed spike width, we additionally tuned the inactivation time constant, $\tau_t = 1.5 \pm 0.5$, for I_{NaT}.

B. *Potassium and leak currents*

The 4-AP sensitive delayed-rectifier type potassium current, I_K, and the leak current, I_{leak} were modeled similar to [8] as below; also see [48].

$$I_K = g_K n(V - E_K)$$

$$I_{leak} = g_{leak}(V - E_{leak})$$

582 where, the steady-state voltage-dependent activation function for the gating variable, n is given as:

583 $$n_\infty(V) = \frac{1}{1 + e^{\left(-(V-43)/3.9\right)}}$$

584 E_K and E_{leak} are K^+ and leak reversal potentials respectively. Model parameter values used are provided
585 in **Supplementary Table. 1**.

586 ***Brain slice preparation***

587 All animal experiments were performed in accordance to the institutional guidelines and
588 regulations using protocols approved by Animal Research Committee at UCLA. Experiments were
589 performed in P8-P14 wild-type mice of either sex. Mice were anesthetized by inhalation of isofluorane
590 and then decapitated. The brainstem was extracted and immersed in ice-cold cutting solution. The brain-
591 cutting solution used during slice preparation was composed of the following (in mM): 194 Sucrose, 30
592 NaCl, 4.5 KCl, 1.2 NaH_2PO_4, 26 $NaHCO_3$, 10 glucose, 1 $MgCl_2$. The extracted brain block was mounted
593 on a vibrating slicer (DSK Microslicer, Ted Pella) supported by an agar block. Coronal brainstem sections
594 consisting of rostro-caudal extent of Mes V nucleus, spanning midbrain and pons were obtained for
595 subsequent electrophysiological recording.

596 ***Voltage-clamp electrophysiology***

597 To obtain direct experimental data to drive I_{NaR} model development, we performed voltage-clamp
598 experiments on Mes V neurons and recorded Na^+ currents by blocking voltage-gated K^+ and Ca^{2+} currents
599 similar to [11]. The pipette internal solution contained the following composition (in mM): 130 CsF, 9 NaCl,
600 10 HEPES, 10 EGTA, 1 $MgCl_2$, 3 K_2-ATP, and 1 Na-GTP. The external recording solution contained the
601 following composition (in mM): 131 NaCl, 10 HEPES, 3 KCl, 10 glucose, 2 $CaCl_2$, 2 $MgCl_2$, 10
602 tetraethylammonium (TEA)-Cl, 10 CsCl, 1 4-aminopyridine (4-AP), and 0.3 $CdCl_2$. The voltage-clamp
603 protocol consisted of a holding potential of -90 mV followed by a brief voltage pulse (3 ms) of +30 mV,

604 to remove voltage-dependent block, followed by voltage steps between -70 mV to -10 mV, in steps of 10
605 mV for ~ 100 ms to activate I_{NaR}, and then returned to -90 mV. A 1 μM TTX abolished the Na^+ current
606 and the residual leak current was subtracted to isolate evident sodium currents. Recordings with series
607 resistance $R_{series} > 0.1R_m$ were discarded, where R_m is the input resistance of the neuron; we did not
608 apply any series resistance compensation.

609 ***Dynamic-clamp electrophysiology***

610 Dynamic-clamp electrophysiology and *in vitro* current-clamp recording were used for testing the
611 physiological effects of Na^+ currents on burst discharge as well as noise-mediated entropy changes
612 corrected by I_{NaR} [51]. We selected neurons responding with a bursting pattern in response to supra-
613 threshold step current injection in the Mes V nucleus in brainstem slice preparation for our study; >50%
614 of neurons showing other patterns (e.g., tonic or single spiking cells) were discarded. Dynamic-clamp was
615 successfully performed in bursting cells (n = 10). For dynamic-clamp recording, slices were placed in
616 normal ACSF at room temperature (22–25°C). The ACSF recording solution during patch-clamp
617 recording consisted of the following (in mM): 124 NaCl, 4.5 KCl, 1.2 NaH_2PO_4, 26 $NaHCO_3$, 10 glucose,
618 2 $CaCl_2$, 1 $MgCl_2$. Cutting and recording solutions were bubbled with carbogen (95% O_2, 5% CO_2) and
619 maintained at pH between 7.25 – 7.3. The pipette internal solution used in current clamp experiments was
620 composed of the following (in mM): 135 K-gluconate, 5 KCl, 0.5 $CaCl_2$, 5 HEPES (base), 5 EGTA, 2 Mg-
621 ATP, and 0.3 Na-ATP with a pH between 7.28 – 7.3, and osmolarity between 290 ± 5 mOsm. Patch
622 pipettes (3 – 5 MΩ) were pulled using a Brown/Flaming P-97 micro pipette puller (Sutter Instruments).
623 Slices were perfused with oxygenated recording solution (~2ml/min) at room temperature while secured
624 in a glass bottom recording chamber mounted on an inverted microscope with differential interface
625 contrast optics (Zeiss Axiovert 10). Current clamp (and dynamic-clamp) data were acquired and analyzed

using custom-made software (G-Patch, Analysis) with sampling frequency: 10 kHz; cut-off filter frequency: 2 kHz.

The Linux-based Real-Time eXperimental Interface (RTXI v1.3) was used to implement dynamic-clamp , running on a modified Linux kernel extended with the Real-Time Applications Interface, which allows high-frequency, periodic, real-time calculations [52]. The RTXI computer interfaced with the electrophysiological amplifier (Axon Instruments Axopatch 200A, in current-clamp mode) and the data acquisition PC, via a National Instruments PCIe-6251 board. Euler's method with step size 0.05 ms was used for model integration resulting in a computation frequency of 20 kHz.

The model I_{NaR} current used for dynamic clamping into Mes V neuron *in vitro* was developed as discussed above. The ionic conductance g_{NaR} was set to suitable values to introduce model I_{NaR} current into a Mes V neuron during whole-cell current-clamp recording. For dynamic-clamp experiments involving g_{NaR} mediated noise modulation, two approaches were used to model random noise I_{noise}, generated in RTXI and injected as pA current:

1) Uniform-distributed random values (white noise):

$$I_{noise}(t) = (U(t) - 0.5) \cdot A$$

where $U(t)$ was a uniformly-distributed random number between 0 and 1 generated by the C^{++} *rand()* function, and A was a scaling factor, in this case determining peak-to-peak noise amplitude. It was varied between 3 and 5, to adjust noise amplitudes to produce discernable burst irregularities. The mean injected noise was 0 pA, and its effective standard deviation varied between 0.87 pA (A=3) and 1.44 pA (A=5).

2) Normally distributed random values (Wiener noise)

$$I_{noise}(t) = I_{noise}(t-1) + N(t) \cdot \sqrt{T} \cdot A$$

where t indicates the value generated at the current computation cycle, and $t-1$ to the value of the previous computation cycle. T was the computation period in seconds (0.00005 s for 20 kHz computation)

649 and was discretized to mimic a Weiner process (random-walk); A was a scaling factor, in this case
650 affecting the noise increment each computation cycle, varying between 3 and 5. $N(t)$ was a normally-
651 distributed random number with mean, $\mu = 0$, and standard deviation, $\sigma = 1$. $N(t)$ was generated from
652 C^{++}-generated uniformly-distributed random numbers using the central limiting theorem:

653 $$N(t) = \left(\sum_{j=1}^{12} U_j \right) - 6$$

654 where each U_j is a uniformly-distributed random number between 0 and 1 generated using the C^{++} *rand()*
655 function. In three 1-second simulations, this noise had mean –0.31±0.19 pA (*A*=3), –0.21±0.62 pA (*A*=4)
656 or –0.59±0.33 pA (*A*=5); and standard deviation 0.77±0.13 pA (*A*=3), 1.07±0.15 pA (*A*=4) or 1.68±0.44
657 pA (*A*=5).

658 We used stochastic current injection as an external input (additive noise) in order to produce
659 irregularities/uncertainties in burst discharge. Our choice of the noise model was to experimentally disrupt
660 spike timing regularity[45] and is not directly based on any known noise characteristics in Mes V neurons.
661 The jaw muscle spindle afferent Mes V neurons are not known to have spontaneous synaptic events and
662 we did not characterize Na+ channel fluctuations in these neurons[53]. Nonetheless, the stochastic noise we
663 used as shown in the representative example in **Fig. 8** most closely matched a diffusive synaptic noise
664 model with Gaussian distribution[54]; **Fig. 8c** illustrates the temporal features of the noise inputs described
665 above. A Gaussian white noise generated in MATLAB with zero mean and unit standard deviation or a
666 Weiner noise generated in XPPAUT were used to disrupt firing patterns in the model neuron.

667 ***Model simulation and Data analyses***

668 Model simulation and all the analyses were performed using MATLAB (Mathworks™) (see model
669 code provided as **Supplementary Information**). Model bifurcation analyses were performed using

XPPAUT/AUTO [55]. A variable step Runge-Kutta method 'ode45' was used for current-clamp simulations and 'ode23s' was used for voltage-clamp simulations.

Inter-event intervals (IEI) between spikes in dynamic-clamp recordings were detected using Clampfit 9.0 software and were classified *post hoc* as ISIs and IBIs based on a bi-modal distribution of IEIs. Typically, IEI values < 40 ms were considered as ISIs within bursts and IEI values ≥ 40 ms were considered as IBIs. Any occasional isolated spikes were eliminated from analyses for burst duration calculations.

To calculate Shannons' entropy[56] in the inter-event intervals (IEIs), we generated histograms of and calculated the probabilities for each bin of the underlying IEI distributions for each 10 sec spike trains. The probability of kth IEI bin from a distribution of n equal size bins was calculated from the bin counts, $N(k)$ as:

$$p(k) = \frac{N(k)}{\sum_{k=1}^{n} N(k)}$$

The entropy, H was calculated using the following formula:

$$H = -\sum_{k=1}^{n} p_k \log_2 p_k$$

where, n is the total number of IEI bins, each with probability, p_k.

The coefficient of variation (CV) in IEIs was calculated as follows:

$$CV = \frac{s}{\bar{x}}$$

where, s is the IEI sample standard deviation, and, $\bar{x}$ is the sample mean.

References

689 1. Krahe, R. & Gabbiani, F. Burst firing in sensory systems. *Nat Rev Neurosci* **5**, 13-23 (2004).
690 2. Ermentrout, B.G. & Terman, D.H. Bursting Oscillations. in *Mathematical Foundations of*
691 *Neuroscience* 103-127 (Springer-Verlag New York, 2010).
692 3. Del Negro, C.A., Hsiao, C.F., Chandler, S.H. & Garfinkel, A. Evidence for a novel bursting
693 mechanism in rodent trigeminal neurons. *Biophys J* **75**, 174-182 (1998).
694 4. Bialek, W., Rieke, F., de Ruyter van Steveninck, R.R. & Warland, D. Reading a neural code.
695 *Science* **252**, 1854-1857 (1991).
696 5. Hodgkin, A.L. & Huxley, A.F. A quantitative description of membrane current and its application
697 to conduction and excitation in nerve. *J Physiol* **117**, 500-544 (1952).
698 6. Catterall, W.A. From ionic currents to molecular mechanisms: the structure and function of
699 voltage-gated sodium channels. *Neuron* **26**, 13-25 (2000).
700 7. Alonso, A. & Llinás, R.R. Subthreshold Na+-dependent theta-like rhythmicity in stellate cells of
701 entorhinal cortex layer II. *Nature* **342**, 175-177 (1989).
702 8. Wu, N.*, et al.* Persistent sodium currents in mesencephalic v neurons participate in burst generation
703 and control of membrane excitability. *J Neurophysiol* **93**, 2710-2722 (2005).
704 9. Hutcheon, B. & Yarom, Y. Resonance, oscillation and the intrinsic frequency preferences of
705 neurons. *Trends Neurosci* **23**, 216-222 (2000).
706 10. Schwindt, P.C. & Crill, W.E. Amplification of synaptic current by persistent sodium conductance
707 in apical dendrite of neocortical neurons. *J Neurophysiol* **74**, 2220-2224 (1995).
708 11. Enomoto, A., Han, J.M., Hsiao, C.F., Wu, N. & Chandler, S.H. Participation of sodium currents
709 in burst generation and control of membrane excitability in mesencephalic trigeminal neurons. *J Neurosci*
710 **26**, 3412-3422 (2006).
711 12. Del Negro, C.A., Koshiya, N., Butera, R.J. & Smith, J.C. Persistent sodium current, membrane
712 properties and bursting behavior of pre-bötzinger complex inspiratory neurons in vitro. *J Neurophysiol*
713 **88**, 2242-2250 (2002).
714 13. Yamanishi, T., Koizumi, H., Navarro, M.A., Milescu, L.S. & Smith, J.C. Kinetic properties of
715 persistent Na. *J Gen Physiol* **150**, 1523-1540 (2018).
716 14. Enomoto, A., Han, J.M., Hsiao, C.F. & Chandler, S.H. Sodium currents in mesencephalic
717 trigeminal neurons from Nav1.6 null mice. *J Neurophysiol* **98**, 710-719 (2007).
718 15. Afshari, F.S.*, et al.* Resurgent Na currents in four classes of neurons of the cerebellum. *J*
719 *Neurophysiol* **92**, 2831-2843 (2004).
720 16. Khaliq, Z.M. & Raman, I.M. Relative contributions of axonal and somatic Na channels to action
721 potential initiation in cerebellar Purkinje neurons. *J Neurosci* **26**, 1935-1944 (2006).
722 17. Raman, I.M. & Bean, B.P. Properties of sodium currents and action potential firing in isolated
723 cerebellar Purkinje neurons. *Ann N Y Acad Sci* **868**, 93-96 (1999).
724 18. Raman, I.M. & Bean, B.P. Resurgent sodium current and action potential formation in dissociated
725 cerebellar Purkinje neurons. *J Neurosci* **17**, 4517-4526 (1997).
726 19. Grieco, T.M., Malhotra, J.D., Chen, C., Isom, L.L. & Raman, I.M. Open-channel block by the
727 cytoplasmic tail of sodium channel beta4 as a mechanism for resurgent sodium current. *Neuron* **45**, 233-
728 244 (2005).
729 20. Raman, I.M., Sprunger, L.K., Meisler, M.H. & Bean, B.P. Altered subthreshold sodium currents
730 and disrupted firing patterns in Purkinje neurons of Scn8a mutant mice. *Neuron* **19**, 881-891 (1997).
731 21. Magistretti, J., Castelli, L., Forti, L. & D'Angelo, E. Kinetic and functional analysis of transient,
732 persistent and resurgent sodium currents in rat cerebellar granule cells in situ: an electrophysiological and
733 modelling study. *J Physiol* **573**, 83-106 (2006).

22. Kim, J.H., Kushmerick, C. & von Gersdorff, H. Presynaptic resurgent Na+ currents sculpt the action potential waveform and increase firing reliability at a CNS nerve terminal. *J Neurosci* **30**, 15479-15490 (2010).
23. Ransdell, J.L.*, et al.* Loss of Navβ4-Mediated Regulation of Sodium Currents in Adult Purkinje Neurons Disrupts Firing and Impairs Motor Coordination and Balance. *Cell Rep* **19**, 532-544 (2017).
24. Browne, L., Smith, K.E. & Jagger, D.J. Identification of Persistent and Resurgent Sodium Currents in Spiral Ganglion Neurons Cultured from the Mouse Cochlea. *eNeuro* **4** (2017).
25. Levin, S.I.*, et al.* Impaired motor function in mice with cell-specific knockout of sodium channel Scn8a (NaV1.6) in cerebellar purkinje neurons and granule cells. *J Neurophysiol* **96**, 785-793 (2006).
26. Seki, S.*, et al.* Pre-symptomatic abnormalities and associated channelopathies in spindle afferent trigeminal mesencephalic V neurons in a SOD1G93A mouse model for Amyotrophic Lateral Sclerosis. in *Society for Neuroscience 2017* (Washington D.C., 2017).
27. Amir, R., Michaelis, M. & Devor, M. Burst discharge in primary sensory neurons: triggered by subthreshold oscillations, maintained by depolarizing afterpotentials. *J Neurosci* **22**, 1187-1198 (2002).
28. Ottolini, M., Barker, B.S., Gaykema, R.P., Meisler, M.H. & Patel, M.K. Aberrant sodium channel currents and hyperexcitability of medial entorhinal cortex neurons in a mouse model of SCN8A encephalopathy. *J Neurosci* (2017).
29. Jarecki, B.W., Piekarz, A.D., Jackson, J.O. & Cummins, T.R. Human voltage-gated sodium channel mutations that cause inherited neuronal and muscle channelopathies increase resurgent sodium currents. *J Clin Invest* **120**, 369-378 (2010).
30. Raman, I.M. & Bean, B.P. Inactivation and recovery of sodium currents in cerebellar Purkinje neurons: evidence for two mechanisms. *Biophys J* **80**, 729-737 (2001).
31. Balbi, P., Massobrio, P. & Hellgren Kotaleski, J. A single Markov-type kinetic model accounting for the macroscopic currents of all human voltage-gated sodium channel isoforms. *PLoS Comput Biol* **13**, e1005737 (2017).
32. Milescu, L.S., Yamanishi, T., Ptak, K., Mogri, M.Z. & Smith, J.C. Real-time kinetic modeling of voltage-gated ion channels using dynamic clamp. *Biophys J* **95**, 66-87 (2008).
33. Milescu, L.S., Yamanishi, T., Ptak, K. & Smith, J.C. Kinetic properties and functional dynamics of sodium channels during repetitive spiking in a slow pacemaker neuron. *J Neurosci* **30**, 12113-12127 (2010).
34. Enomoto, A.*, et al.* Development of resurgent and persistent sodium currents in mesencephalic trigeminal neurons. *J Neurosci Res* (2017).
35. Wu, N., Hsiao, C.F. & Chandler, S.H. Membrane resonance and subthreshold membrane oscillations in mesencephalic V neurons: participants in burst generation. *J Neurosci* **21**, 3729-3739 (2001).
36. Yang, J.*, et al.* Membrane current-based mechanisms for excitability transitions in neurons of the rat mesencephalic trigeminal nuclei. *Neuroscience* **163**, 799-810 (2009).
37. Khaliq, Z.M., Gouwens, N.W. & Raman, I.M. The contribution of resurgent sodium current to high-frequency firing in Purkinje neurons: an experimental and modeling study. *J Neurosci* **23**, 4899-4912 (2003).
38. Birmingham, J.T., Szuts, Z.B., Abbott, L.F. & Marder, E. Encoding of muscle movement on two time scales by a sensory neuron that switches between spiking and bursting modes. *J Neurophysiol* **82**, 2786-2797 (1999).
39. Zheng, Y. & Escabí, M.A. Proportional spike-timing precision and firing reliability underlie efficient temporal processing of periodicity and envelope shape cues. *J Neurophysiol* **110**, 587-606 (2013).

40. Reich, D.S., Mechler, F., Purpura, K.P. & Victor, J.D. Interspike intervals, receptive fields, and information encoding in primary visual cortex. *J Neurosci* **20**, 1964-1974 (2000).
41. Tiesinga, P., Fellous, J.M. & Sejnowski, T.J. Regulation of spike timing in visual cortical circuits. *Nat Rev Neurosci* **9**, 97-107 (2008).
42. Mainen, Z.F. & Sejnowski, T.J. Reliability of spike timing in neocortical neurons. *Science* **268**, 1503-1506 (1995).
43. Vilin, Y.Y. & Ruben, P.C. Slow inactivation in voltage-gated sodium channels: molecular substrates and contributions to channelopathies. *Cell Biochem Biophys* **35**, 171-190 (2001).
44. Béhuret, S., Deleuze, C. & Bal, T. Corticothalamic Synaptic Noise as a Mechanism for Selective Attention in Thalamic Neurons. *Front Neural Circuits* **9**, 80 (2015).
45. Faisal, A.A., Selen, L.P. & Wolpert, D.M. Noise in the nervous system. *Nat Rev Neurosci* **9**, 292-303 (2008).
46. Izhikevich, E.M., Desai, N.S., Walcott, E.C. & Hoppensteadt, F.C. Bursts as a unit of neural information: selective communication via resonance. *Trends Neurosci* **26**, 161-167 (2003).
47. Lisman, J.E. Bursts as a unit of neural information: making unreliable synapses reliable. *Trends Neurosci* **20**, 38-43 (1997).
48. Del Negro, C.A. & Chandler, S.H. Physiological and theoretical analysis of K+ currents controlling discharge in neonatal rat mesencephalic trigeminal neurons. *J Neurophysiol* **77**, 537-553 (1997).
49. Taddese, A. & Bean, B.P. Subthreshold sodium current from rapidly inactivating sodium channels drives spontaneous firing of tuberomammillary neurons. *Neuron* **33**, 587-600 (2002).
50. Smith, M.R., Smith, R.D., Plummer, N.W., Meisler, M.H. & Goldin, A.L. Functional analysis of the mouse Scn8a sodium channel. *J Neurosci* **18**, 6093-6102 (1998).
51. Prinz, A.A., Abbott, L.F. & Marder, E. The dynamic clamp comes of age. *Trends Neurosci* **27**, 218-224 (2004).
52. Lin, R.J., Bettencourt, J., Wha Ite, J., Christini, D.J. & Butera, R.J. Real-time experiment interface for biological control applications. *Conf Proc IEEE Eng Med Biol Soc* **2010**, 4160-4163 (2010).
53. Verdier, D., Lund, J.P. & Kolta, A. Synaptic inputs to trigeminal primary afferent neurons cause firing and modulate intrinsic oscillatory activity. *J Neurophysiol* **92**, 2444-2455 (2004).
54. Fourcaud-Trocmé, N., Hansel, D., van Vreeswijk, C. & Brunel, N. How spike generation mechanisms determine the neuronal response to fluctuating inputs. *J Neurosci* **23**, 11628-11640 (2003).
55. Ermentrout, B. XPPAUT5.0 – the differential equations tool. (2001).
56. Shannon, C.E. & Weaver, W. *The Mathematical Theory of Communication* (University of Illinois Press, Urbana, 1949).

Supplementary Information

4 Supplementary figures and legends
2 Tables
1 piece of Supplementary information providing the *Model analyses using dynamical systems methods*

Supplementary Figure Legends

Supplementary Figure 1. a) A state-based Markov model for I_{Na} as in Raman & Bean (2001). C1 to C5 represent sequential closed states and O denotes the open state. I1 through I6 represent the inactivation states for the normal inactivation mechanism. The rate constants in ms^{-1} are: $\alpha = 190e^{(V/20)}$, $\beta =$

$1.6e^{(-V/19.5)}$, $\gamma = 190$, and, $\delta = 41$. The normal inactivation is voltage-independent and occurs with rate constants, C_{on} = 0.002 ms^{-1}, C_{off} =0.53 ms^{-1}, while the O_{on} and O_{off} are 0.2 and 0.003 ms^{-1} respectively. The binding factor 'a' for the inactivating particle is given by $(C_{off}/C_{on})/(O_{off}/O_{on}))^{1/8}$. The rate constant ε = 1.75 ms^{-1}, is the rate at which the open channel block occurs and the exit from the blocked state is modeled as a voltage-dependent process given by $\zeta = 0.03e^{4/67}$ ms^{-1}. **b)** Voltage-clamp simulation of the Markov model shows the resurgent sodium current; Protocol is shown in the inset; Also highlighted are the transient and persistent components. **c)** The sodium current generated during action potentials both in our three-component Hodgkin-Huxley (3HH) type model and the Markov model are shown for comparison; spikes are in blue and sodium current is in red.

Supplementary Figure 2. a) Model simulation of sodium channel recovery and its relationship with resurgent current flow. Upper traces in **(a)** and **(b)** show two voltage-clamp protocols with voltages as shown; Δt represents variable intervals from 3 – 39 ms for the test voltage of -40 mV; lower traces show the corresponding current responses. **c)** Percent channel availability calculated as the peak current at the test steps to -40 mV, normalized to the peak current at the reference pulse of 0 mV; **d)** Steady-state availability, calculated as peak current evoked at 0 mV following a 200 ms pre-pulse conditioning steps (-90 to +30 mV), normalized by the peak current at 0 mV following conditioning at -90 mV.

Supplementary Figure 3. a) Rise and decay kinetics in the model (magenta) and experimental trace (black) at a test potential of -40 mV where maximum resurgent current is seen. **b, c)** Rise and decay times for the model and experiments (n=5) are shown for three test potentials at which a sizable current was seen in ≥ 50% of the time; Rise time was calculated from 10 – 90% of the peak value, and, decay time was calculated from 90 – 10% of steady-state value at the end of the test pulse. Error bars indicate standard deviation.

Supplementary Figure 4. a, c) Representative burst discharge showing the effects of dynamic-clamp subtraction of g_{NaR} **(a)** and g_{NaP} **(c)**; decreasing values of 0.25 and 0.5 nS/pF, and 0.05 and 0.1 nS/pF were used for 1X and 2X g_{NaR} and g_{NaP} respectively. Red double arrows highlight inter-burst intervals (IBIs). The magenta rectangles and the corresponding numbers are shown in expanded time and voltage in the boxed inset to highlight abolition of STO due to g_{NaP} subtraction (compare upper and middle traces in the box), which was further comparable to setting $g_{NaP} = 0$ in neuron model simulations (lower trace). **a, c)** Box plots showing effects of g_{NaR} **(b)** and g_{NaP} **(d)** subtraction on inter-spike intervals (ISIs) within bursts; C is control. A one-way ANOVA for treatment effect on ISIs had a $p < 0.001$ for g_{NaR} subtraction, with no significant effect of g_{NaP} between C and -1x; however, all spikes were abolished upon -2x g_{NaP} application. Asterisks in **(b)** indicate statistical significance with $p < 0.001$ using a Student t-test for group comparisons (Control v/s -1x and -1x v/s -2x).

Supplementary Text

Bifurcation Analyses of Model Behavior

Mathematical analytical approaches enable examination of experimentally intractable mechanisms and provide deeper insights into the behavior of complex nonlinear dynamical systems. We combined model simulations with geometric dynamical systems methods to examine the I_{NaR}'s mechanism of burst control. In this supplementary text, we explain the theoretical concepts underlying the so-called

bifurcation diagrams presented in **Figs. 6d** and **e**. First, to generate theses diagrams, we dissected the system of equations representing the bursting neuron model into fast and slow subsystems[2]. This enabled understanding the qualitative changes in the behavior of fast subsystem consisting of the membrane potential (V) due to changes in the slow kinetics of persistent Na^+ inactivation/recovery (h_p) (see **Figs. 6a-c** highlighting relative timescales of V and h_p during bursting activity). Note that during a burst of activity, h_p is inactivating (decreasing) during each spike, however, recovers from inactivation on a relatively slow timescale. In the diagrams in **Figs. 6d** and **e**, we treat the slow variable h_p as a parameter that when slowly changes, causes qualitative changes in the fast variable, V. For example, we can determine for which values of h_p the fast subsystem generates either near rest behavior or quiescence (stable equilibria) or spikes (stable oscillations) or both. Note that there are two values of h_p, h_{HB} (onset threshold) and h_{SNP} (offset threshold), such that V exhibits: i) a near rest behavior (stable equilibrium – red curve) for $h_p < h_{HB}$; ii) an unstable equilibrium for $h_p > h_{HB}$; and iii) spiking for $h_p < h_{SNP}$ (stable oscillations – green circles). As h_p gradually increases during IBI, indicating channel recovery, the membrane potential, V transitions from a resting state (or stable equilibria) until it reaches the Andronov-Hopf bifurcation point, labeled "onset threshold" (e.g., **Figs. 6d**), that is representative of spike onset threshold. Past this threshold, V becomes unstable and spiking phase begins whose amplitudes are bounded by the upper and lower green curves marking the maximum (peak) and minimum (trough) values of membrane potential, V. These represent stable oscillations (or periodic solution) when the neuron is in the bursting phase. For, $h_{SNP} < h_p < h_{HB}$, the membrane potential, V shows bistability: for those values of h_p, there is both a stable equilibrium and a stable oscillation. The same diagrams are reproduced for specific g_{NaR} and g_{NaP} values in **Figs. 7d-f** where the green shaded region that represents a region of attraction for the stable curve of equilibria are highlighted. Physiologically, this region houses the sub-threshold oscillations that decay in amplitude as a burst terminates.